

**Università degli Studi di Napoli “Federico II”**



**SCUOLA POLITECNICA E DELLE SCIENZE DI BASE  
DIPARTIMENTO DI INGEGNERIA INDUSTRIALE**

**CORSO DI LAUREA IN INGEGNERIA AEROSPAZIALE  
CLASSE DELLE LAUREE IN INGEGNERIA INDUSTRIALE (L-9)**

Elaborato di laurea in Meccanica del Volo

**Geometric modelling, stability and control analysis  
of the unmanned aerial vehicle Northrop Grumman  
RQ-4 Global Hawk with OpenVSP**

**Relatore:**  
**Prof. Danilo Ciliberti**

**Candidato:**  
**Christian Mocogni**  
**Matr. N35004492**

**ANNO ACCADEMICO 2023 – 2024**

*A chi c'è sempre stato.*

*A chi se n'è andato.*

*A mia madre, mia sorella e mia nonna.*

*A tutti coloro che hanno creduto in me fin dall'inizio*

*E fino alla fine.*

*A te, che più di tutti avresti voluto essere qui oggi.*

*A mio padre, Filippo.*

# Table of contents

1.	Introduction .....	8
1.1	Objective.....	8
1.2	Layout of work .....	8
1.3	Northrop Grumman RQ-4 Global Hawk .....	9
1.3.1	Northrop Grumman RQ-4 Global Hawk .....	9
1.3.2	UAV flight stability and stability derivatives.....	10
2.	Vortex Lattice Method .....	11
2.1	Theoretical Background .....	12
2.1.1	Boundary Conditions.....	12
2.1.2	Biot-Savart Law.....	13
2.1.3	Implementation in VSPAero .....	14
3.	Geometric Modelling .....	16
3.1	OpenVSP .....	16
3.1.1	VSPAERO.....	17
3.2	Global Hawk modelling .....	18
3.2.1	Wing .....	19
3.2.2	Fuselage .....	21
3.2.3	V – Tailplane .....	22
4.	Results and longitudinal aerodynamic analysis .....	23
4.1	Aerodynamic curves .....	24
4.2	Neutral Point.....	30
4.3	Effects of control surfaces on Longitudinal Stability .....	31
4.3.1	Flaps .....	32
4.3.2	Ruddervators with symmetrical deflections .....	36
4.4	Lateral and Directional Stability Aerodynamics Analysis .....	39

4.4.1	Aircraft behavior without control surfaces deflected .....	39
4.4.2	Ailerons effect on Lateral and Directional stability .....	40
4.4.3	Ruddervators effect on Lateral and Directional stability.....	44
5.	Conclusion.....	47
	Bibliography .....	48

# List of figures

Figure 1.1 The Northrop Grumman RQ-4 Global Hawk.	9
Figure 1.2 Stability conditions in pitch, roll and yaw.	11
Figure 2.1 Working principle used by the VLM.	13
Figure 2.2 Flow induced by vortex filament.	14
Figure 3.1 OpenVSP working window and geometry browser.	16
Figure 3.2 Northrop Grumman RQ-4 Globalhawk reference.	18
Figure 3.3 GlobalHawk seen from four point of view in OpenVSP.	19
Figure 3.4 Wing and wing geometry window.	19
Figure 3.5 Wing airfoil profile (NASA LRN 1015).	20
Figure 3.6 Tessellation adjustment bar.	20
Figure 3.7 Proportional distribution of the slices between section 2 and 3.	21
Figure 3.8 Fuselage geometry window.	22
Figure 3.9 Tailplane geometry window.	22
Figure 3.10 Tailplane symmetrical airfoil profile (NACA 0010).	23
Figure 4.1 VSPAero and set selection panels.	23
Figure 4.2 Lift coefficient curves for the three sets of components.	25
Figure 4.3 Pitching moment coefficient curves.	27
Figure 4.4 Trailing wakes at $\alpha = 4^\circ$ .	27
Figure 4.5 Trailing wakes at $\alpha = 8^\circ$ .	28
Figure 4.6 Aerodynamic Efficiency curves	28
Figure 4.7 Parasite Drag tool results.	29
Figure 4.8 CL vs CD and CD <sub>i</sub> curves.	29
Figure 4.9 Flaps and Ailerons.	31

Figure 4.10 Ruddervators .....	32
Figure 4.11 Lift coefficient curves for flap deflections of $0^\circ$ , $15^\circ$ , $30^\circ$ .....	33
Figure 4.12 Trailing wakes with flaps deflections of $15^\circ$ . .....	34
Figure 4.13 Trailing wakes with flaps deflections of $30^\circ$ . .....	34
Figure 4.14 Pitching moment coefficient curves for flap deflections of $0^\circ$ , $15^\circ$ and $30^\circ$ . ....	35
Figure 4.15 Lift coefficient curves for ruddervators symmetrical deflections of $+10^\circ$ , $0^\circ$ , $-10^\circ$ , $-20^\circ$ and $-30^\circ$ .....	36
Figure 4.16 Trailing wakes for ruddervators deflections, for each $\delta r$ . ....	37
Figure 4.17 Pitching moment coefficient curves for for ruddervators symmetrical deflections of $+10^\circ$ , $0^\circ$ , $-10^\circ$ , $-20^\circ$ and $-30^\circ$ .....	38
Figure 4.18 Lateral and Directional Natural Response of the aircraft with $\beta$ variations.....	39
Figure 4.19 $C\ell$ vs $\delta a$ .....	41
Figure 4.20 $C_n$ vs $\delta a$ .....	42
Figure 4.21 Trend lines of $C_n$ vs $\delta a$ .....	42
Figure 4.22 Trailing wakes with ailerons deflections of $0^\circ$ , $10^\circ$ , $20^\circ$ , $30^\circ$ .....	43
Figure 4.23 $C\ell$ vs $\delta r$ . .....	44
Figure 4.24 $C_n$ vs $\delta r$ . .....	45
Figure 4.25 Rear view of Trailing wakes for Ruddervators Antisymmetrical deflections of $0^\circ$ , $10^\circ$ , $20^\circ$ , $30^\circ$ . .....	46

## List of tables

Table 4.1 Lift coefficients for the wing, wing and tail, complete aircraft.....	24
Table 4.2 Pitching moment coefficients for the wing, wing and tail, complete aircraft. ....	26
Table 4.3 Lift coefficient for flap deflections of $0^\circ$ , $15^\circ$ , $30^\circ$ . .....	33
Table 4.4 Pitching moment coefficient values for flap deflections of $0^\circ$ , $15^\circ$ and $30^\circ$ .....	35
Table 4.5 Lift coefficient for ruddervators symmetrical deflections of $+10^\circ$ , $0^\circ$ , $-10^\circ$ , $-20^\circ$ and $-30^\circ$ .....	36
Table 4.6 Pitching moment coefficient values for for ruddervators symmetrical deflections of $+10^\circ$ , $0^\circ$ , $-10^\circ$ , $-20^\circ$ and $-30^\circ$ .....	38
Table 4.7 Natural Response of the aircraft with $\beta$ variations. ....	39
Table 4.8 Rolling moment coefficient with ailerons deflections of $0^\circ$ , $10^\circ$ , $20^\circ$ and $30^\circ$ .....	40
Table 4.9 Yawing moment coefficient with ailerons deflections of $0^\circ$ , $10^\circ$ , $20^\circ$ and $30^\circ$ .....	41
Table 4.10 Rolling moment coefficient with ruddervators asymmetric deflections of $0^\circ$ , $10^\circ$ , $20^\circ$ and $30^\circ$ .....	44
Table 4.11 Yawing moment coefficient with ruddervators asymmetric deflections of $0^\circ$ , $10^\circ$ , $20^\circ$ and $30^\circ$ .....	45

# **Abstract**

This work focuses on the geometric modeling and analysis of stability and control characteristics of a remotely piloted aircraft (UAS – Unmanned Aerial System), specifically the RQ-4 Global Hawk, an UAV designed for high-altitude, long-endurance surveillance missions. The study was conducted using OpenVSP, an open-source software developed by NASA for parametric aircraft modeling. The geometry of the RQ-4 was accurately reproduced in OpenVSP, allowing for a precise definition of the aerodynamic surfaces. Subsequently, the VSPAERO module, integrated into the aforementioned software, was employed for stability and control analysis. This tool is based on Vortex Lattice Method to estimate the aerodynamic properties of the aircraft, such as lift, drag, moments, and stability derivatives. The lifting surfaces were modeled as infinitely thin curved surfaces with discrete vortices. The analysis allowed for the evaluation of the RQ-4's static stability conditions, highlighting the aircraft's behavior in different flight configurations. Despite its limitations for more complex models, the tool proved to be a convenient solution for simple designs requiring preliminary numerical analysis.

# **Sommario**

Il presente lavoro si concentra sulla modellazione geometrica e sull'analisi delle caratteristiche di stabilità e controllo di un velivolo a controllo remoto (UAS – Unmanned Aerial System), in particolare del RQ-4 Global Hawk, un UAV progettato per missioni di sorveglianza ad alta quota e lunga durata. Il lavoro è stato svolto utilizzando OpenVSP, un software open-source sviluppato dalla NASA per la modellazione parametrica di velivoli. La geometria del RQ-4 è stata riprodotta fedelmente in OpenVSP, permettendo un'accurata definizione delle superfici aerodinamiche. Successivamente, per l'analisi di stabilità e controllo è stato utilizzato il modulo VSPAERO, un tool integrato nel suddetto programma basato sul Vortex Lattice Method per stimare le proprietà aerodinamiche del velivolo, come portanza, resistenza, momenti e derivate di stabilità. Le superfici portanti sono state modellate come superfici curve infinitamente sottili di vortici discreti. L'analisi condotta ha permesso di valutare le condizioni di stabilità statica del velivolo RQ-4, evidenziando il comportamento del velivolo in diverse configurazioni di volo. Nonostante i suoi limiti per modelli più complessi, lo strumento si è dimostrato essere una soluzione conveniente per design semplici che necessitano di un'analisi numerica preliminare.

# 1. Introduction

## 1.1 Objective

The objective of this work is to completely portray the aerodynamic and stability analysis of the unmanned aerial vehicle Northrop Grumman RQ-4 Global Hawk. The findings obtained from this study are a preliminary data set, as both VSPAERO and the Vortex Lattice Method present their limits, therefore they can only be used as a first evaluation of aerodynamic performance, stability, and control. Moreover, the thesis aims to clarify the VLM numerical method, its fundamental theory, and how it is implemented by the software used. The under-analysis of UAV's characteristic curves and other valuable data, such as the lift, aerodynamic efficiency, moment coefficients, and drag polar curves for the isolated wing, partial and complete aircraft, were obtained via Microsoft Excel data processing. Lastly, the aircraft's static stability characteristics were evaluated from the collected data.

## 1.2 Layout of work

**Chapter 1:** In this chapter is shown a brief introduction of the vehicle and a presentation of basics UAV information.

**Chapter 2:** This chapter illustrates the core assumptions behind the Vortex Lattice Methods and their consequences.

**Chapter 3:** In this chapter the OpenVSP software will be presented along with the tools used for this work as well as illustrating how the model has been created.

**Chapter 4:** In this final chapter the results are presented and analysed to deduce information regarding the stability and control of the vehicle.

## 1.3 Northrop Grumman RQ-4 Global Hawk

### 1.3.1 Northrop Grumman RQ-4 Global Hawk

The Northrop Grumman RQ-4 Global Hawk is a remotely piloted aircraft (UAV, Unmanned Aerial Vehicle) designed for strategic reconnaissance and surveillance missions. Developed and manufactured by Northrop Grumman, the Global Hawk represents one of the most advanced surveillance platforms in the world, primarily used by the US Air Force and NASA. Its development began in the 1990s as part of the American program to modernize long-range and high-altitude intelligence capabilities.



**Figure 1.1 The Northrop Grumman RQ-4 Global Hawk.**

The Global Hawk is a large aircraft, with a wingspan of approximately 40 meters, a length of 14.5 meters, and a height of 4.7 meters. This aircraft is capable of flying at extremely high altitudes, up to 65,000 feet, well above the reach of conventional commercial or military aircraft. It is equipped with advanced surveillance sensors, including:

- **Active electronically scanned array (AESA) radar** for high-resolution ground imaging, at night or even in adverse weather conditions;
- **Electro-optical and infrared sensors** for day and night visual observation;
- **SIGINT sensors** for intercepting and analyzing electronic signals;

The Global Hawk can fly for over 30 consecutive hours without refueling, covering vast distances without any interruptions.

The primary use of the RQ-4 is in the military field, where it conducts long-range surveillance missions to provide real-time information to operational commands. It has been deployed in numerous operations, including the conflicts in Iraq and Afghanistan, as well as for monitoring sensitive areas such as the Korean Peninsula and the Middle East.

NASA also uses the Global Hawk for high-altitude scientific missions, such as monitoring climate change, studying atmospheric composition, and observing extreme weather phenomena like hurricanes [1].

### *1.3.2 UAV flight stability and stability derivatives*

Stability is defined as the tendency of the UAV to return to a condition of equilibrium when subjected to a disturbance in flight, typically caused by gusts or flight control input. Specifically static stability, which can be positive, negative, divergent or neutral, is the initial response of the aircraft to regain equilibrium upon a disturbance [2][2]. The Neutral Point (NP) is the location of the aircraft's centre of gravity (CG) that would result in neutral static longitudinal stability. The stability criterion is expressed in terms of the aircraft's static margin (SM), which is the distance between the CG and the NP in body axes and defined as a non-dimensional measure of the aircraft's stability, since the longitudinal stability heavily depends on the CG's location. The aircraft is neutral with respect to longitudinal rotation (pitch) when the CG is located at the aircraft's neutral point, stable when the CG is positioned ahead of the NP, and unstable when moved aft. A high SM may denote a fairly stable but not particularly manoeuvrable aircraft, while UAV with high manoeuvrability have a low stability or even be statically unstable.

During flight, moments on a UAV are created by the aerodynamic load distribution and the thrust force not acting through the CG. Aerodynamic moments are expressed in terms of the dimensionless coefficients for pitching moment ( $C_M$ ), rolling moment ( $C_\ell$ ) and yawing moment ( $C_N$ ). The values of  $C_M$ ,  $C_\ell$ , and  $C_N$  depend on the angle of attack ( $\alpha$ ), Reynolds number (Re), Mach number (M), and sideslip angle ( $\beta$ ). They are functions of the angular rates and sideslip of the aircraft. A necessary condition for longitudinal static stability of the UAV is that the

pitching moment curve has a negative slope through the equilibrium point. Also, the slope must be negative for lateral static stability and positive for directional static stability. These criteria are valid for a body reference frame (Figure 1.2 and Figure 1.3).

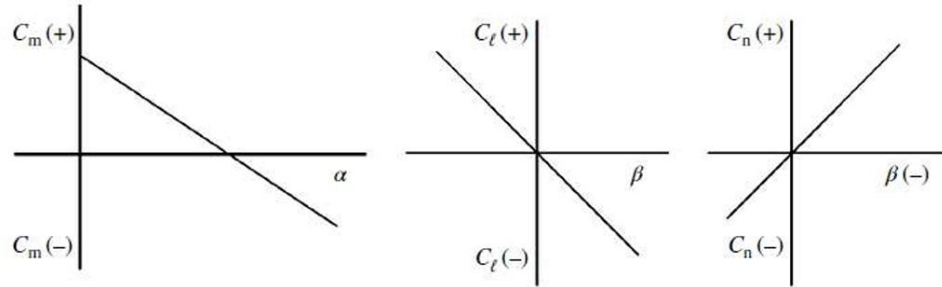


**Figure 1.2 Stability conditions in pitch, roll and yaw.**

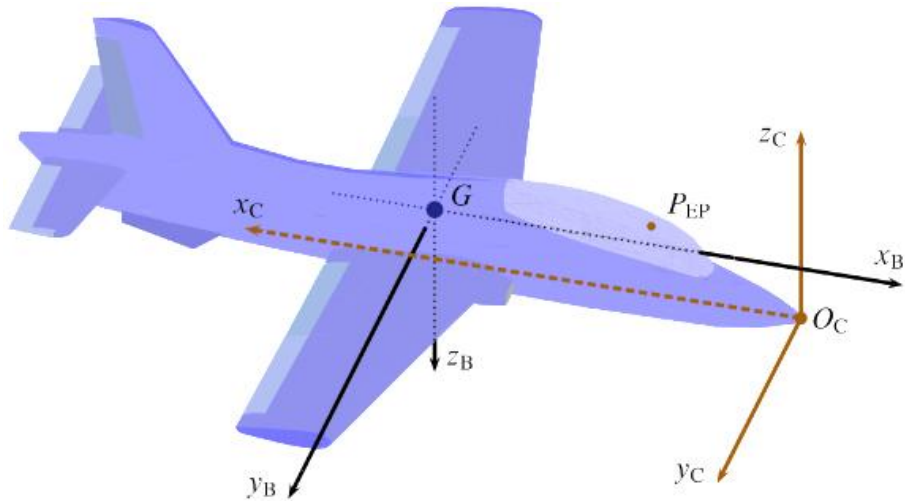


**Figure 1.3 Body Reference Frame and Constructive Reference Frame.**

## 2. Vortex Lattice Method

The vortex lattice method is a computational fluid dynamic technique to estimate aerodynamic load distribution and thus forces and moments acting on the aircraft. It is very useful in the preliminary stages of aircraft design. The method operates on the foundation of an incompressible, inviscid, and irrotational flow field, which is accurately represented by

Laplace's equation. Furthermore, the angles of attack and sideslip are assumed to be small and the lifting surfaces are thin, neglecting the effects of thickness on aerodynamic forces.

## 2.1 Theoretical Background

As previously said, the flow is irrotational, which means that the vorticity is null at every point:

$$\xi = \nabla \times V = 0 \quad \text{Equation 2.1}$$

Defining  $\varphi$  as a scalar function, we get:

$$\nabla \times (\nabla \varphi) = 0 \quad \text{Equation 2.2}$$

Combining the previous two formulas:

$$V = \nabla \varphi \quad \text{Equation 2.3}$$

which asserts that for an irrotational flow, there exists a scalar function  $\varphi$  such that the velocity is determined by the gradient of said function, hence the term velocity potential. Applying the mass conservation principle for an incompressible flow:

$$\nabla \cdot V = 0 \quad \text{Equation 2.4}$$

Having previously defined the velocity potential, integrating (2.3) and (2.4) yields to:

$$\nabla \cdot (\nabla \varphi) = 0 \quad \text{Equation 2.5}$$

or

$$\nabla \varphi = 0$$

namely the Prandtl-Glauert equation, which governs this irrotational and incompressible flow. Because irrotational and incompressible flow is a complicated flow pattern, its solution can be expressed as the sum of a number of elementary irrotational and incompressible flows.

### 2.1.1 Boundary Conditions

The vortex lattice method employs the linearization and transfer of the boundary condition, in addition to the linear approximation of velocity and pressure, known as the thin airfoil boundary condition. This allows for the influence of thickness and viscosity to be neglected.

The significance of this analysis is that the cambered surface boundary conditions could even be applied on a flat coordinate surface, resulting in a much easier approach for implementing the boundary conditions. Once applied to the Laplace's equation, considering a symmetrical airfoil, the camber effect can also be disregarded, and the problem can be simply solved by considering the effect of angle of attack on a flat surface. This is the working principle VLM employs [6].

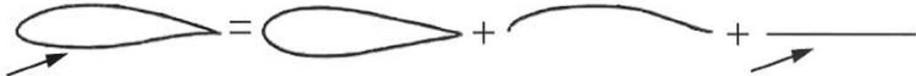


**Figure 2.1 Working principle used by the VLM.**

Considering a wing, according to the boundary conditions, the normal flow across the thin wing's solid surface is zero:

$$\nabla(\varphi + \varphi_\infty) = 0 \quad \text{Equation 2.6}$$

which implies that the sum of the normal velocity components induced by the wing's bound vortices  $w$ , the wake  $w$ , and the free-stream velocity  $v_\infty$  will be zero.

$$w_b + w_i + v_\infty \cdot \alpha = 0 \quad \text{Equation 2.7}$$

### 2.1.2 Biot-Savart Law

One of the possible solutions to Laplace's equation is the two-dimensional vortex singularity.

The flow induced by this filament is outlined by the Biot-Savart law:

$$dV_p = \frac{\Gamma}{4\pi} \cdot \frac{dl \times r_p}{|r_p|^2} \quad \text{Equation 2.8}$$

The induced velocity  $dV_p$  at a point P, due to a segment of a vortex filament  $dl$  at a point  $q$  is directly proportional to the vortex strength  $\Gamma$  (which has the same sign as the vorticity, positive if clockwise) and inversely proportional to the square of the distance  $r_p$ .

The concept of a point vortex can be extended to the case of a general three-dimensional vortex filament, its induced flow field is shown in figure (2.2). The induced velocity is obtained by integrating along the entire length of the vortex filament.

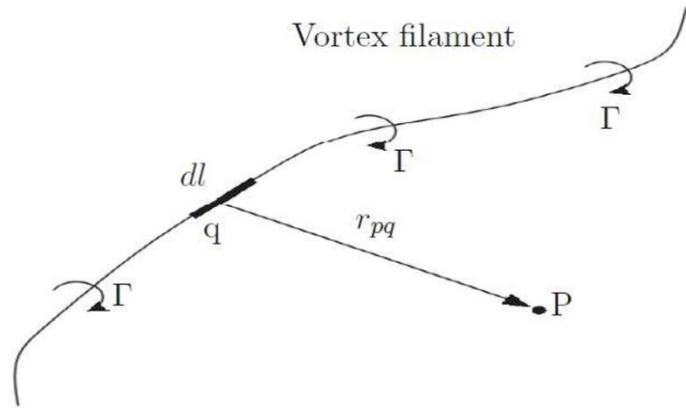


**Figure 2.2 Flow induced by vortex filament.**

### 2.1.3 Implementation in VSPAero

The geometry is approximated using various lifting surface simplifications. For fuselages, a simplified representation, referred to as the “cruise department model” is employed. This model utilizes longitudinal and lateral approximations to capture the planform shape in both views. The resulting computational mesh consists of a mixture of polygons, commonly referred to as the *vortex lattice model*. It is important to note that thickness is disregarded in all geometrical approximations.

In this approach, the aircraft geometry is intersected, and internal components are removed to obtain the wetted area of the vehicle. The final mesh, referred to as a *panel model*, is composed of polygons without any approximations in terms of geometry.

Both *DegenGeom* and *CompGeom* models produce computational meshes comprised of polygons that can be utilized in aerodynamic solvers, including:

1. **Navier-Stokes equations:** providing a detailed and realistic representation of aerodynamic flows.
2. **Euler equations:** offering a less computationally intensive alternative.
3. **Panel methods:** focusing on incompressible flows for rapid computation.

#### 4. Vortex Lattice Methods (VLM): neglecting thickness and focusing solely on planform effects.

In both *Panel Methods* and *VLM*, vortex rings are distributed over the vehicle geometry. The strength of these vortex rings is determined to ensure that the induced velocity at the centroid of each ring is tangent to the local surface geometry. This condition prevents flow from penetrating the surface of the model.

Wake vortices, originating from sharp trailing edges, are modeled as vortex lines. The strength and location of these lines are determined iteratively by enforcing the Kutta condition, which ensures smooth flow detachment from the trailing edges. The vortex lines are positioned to align with the streamlines of the overall flow field.

The solver models the geometry as a collection of polygons, primarily favoring regular quadrilateral and triangular shapes for computational efficiency. The induced velocity of each vortex ring is determined using the generalized Biot-Savart law, which is based on the circulation strength of the vortex. While the Biot-Savart integral is stable for subsonic flows, supersonic flows introduce additional mathematical complexities due to the nature of the flow.

Each vortex ring, typically evaluated at its centroid, requires the calculation of induced velocity contributions from all other vortex rings and trailing wakes, as well as external influences such as free-stream velocity and rotor effects. The total induced velocity at a given point, when combined with these contributions and projected along the normal vector of the vortex ring, must satisfy a zero normal velocity condition, which serves as the boundary condition.

This leads to a linear system of equations expressed as  $A\Gamma = b$ , where  $\Gamma$  represents the circulation strengths of the vortex loops, and it is determined by the boundary condition. Solving this system provides the vortex strengths necessary to enforce the boundary conditions. The strengths of the wake vortices are defined in terms of the body vortex strengths, avoiding the introduction of additional unknowns [4].

### 3. Geometric Modelling

#### 3.1 OpenVSP

Open Vehicle Sketchpad (OpenVSP) is an open-source parametric aircraft geometry, originally developed by Dave Kinney at NASA Ames. It enables the user to build three dimensional models of aircrafts from common engineering parameters and the models obtained can be then processed in formats suitable for structural or aerodynamic analysis. The website can be accessed via the following link: <https://openvsp.org>

Upon launch, Open VSP displays a working window as well as a Geometry browser (Figure 3.1), the latter can be used to add all the individual components that make up an airplane. It also provides multiple basic aircraft geometry shapes, that can be altered utilizing the component geometry window, and can easily combined into an aircraft model.

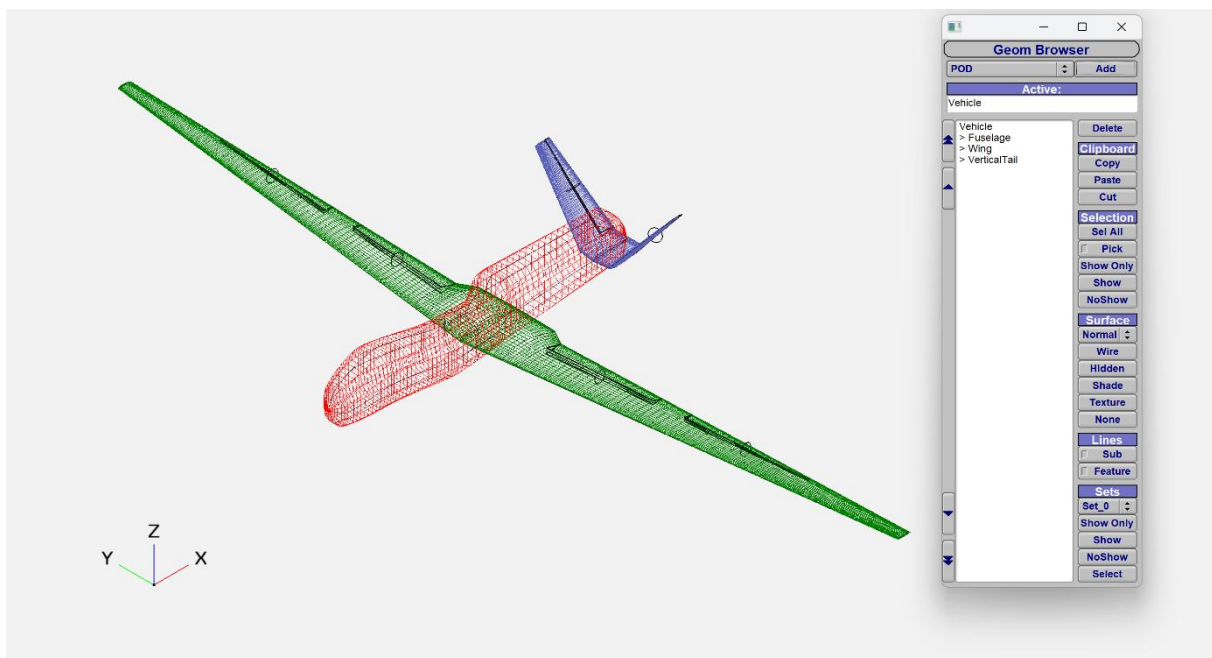


*Figure 3.1 OpenVSP working window and geometry browser.*

### 3.1.1 VSPAERO

VSPAERO is a tool provided by OpenVSP; it is a thin-surface code for inviscid subsonic and supersonic aerodynamics. It incorporates a single actuator disk model to depict the interaction of propulsion and aircraft, as well as the ability to calculate common stability derivatives.

VSPAERO fails to simulate stall or separation characteristics as it is a linear solver. It has integrated actuator disks that can be precisely specified for rapid and straightforward aero-propulsive study. It includes a Viewer tool that displays wakes and the change in pressure coefficient.

The control grouping VSPAERO GUI tab facilitates the construction of groups of control surfaces in the VSPAERO configuration file. All rectangular surfaces and control subsurfaces that can be added to a group are listed in the Available Control Surfaces browser. Subsurface gains can be altered to allow control surfaces within a group to be mixed.

The VSPAERO's vortex lattice solver requires the degenerate geometry file, a three-dimensional model representation in progressively simpler frames. First, the entire three-dimensional model is represented, followed by a plane representation, and then by a stick representation.

In order to start the analysis, operational conditions must be defined. The provided drag output mainly contains information about the induced drag. Using components in the DegenGeom build file that do not affect lift, such as the nacelle and fuselage, may result in increased operating time with no valuable return in terms of lift and drag, while it should provide their effect on the aerodynamic moments. When utilizing this tool, the lift surfaces, such as the wing and horizontal stabilizer, are the major components that affect the output values. These files can be opened with text editors or spreadsheets.

Although the minor impact other components have on the vehicle's aerodynamic drag, the generated drag determined by VSPAERO is mostly based on the lift coefficient. When running the vortex lattice method, VSPAERO will generate a number of files containing critical information for model analysis. The software collects the data in text files that can be then elaborated in spreadsheets. The files used in this work are POLAR files for global aircraft's coefficients and finally STAB files for control and stability derivatives.

### 3.2 Global Hawk modelling

In this chapter we briefly illustrate how the model has been constructed with the tools above mentioned, from the basic wing geometry to the fuselage and the tailplane as well as the control surfaces. Figure depicts the reference utilized to realize this model.

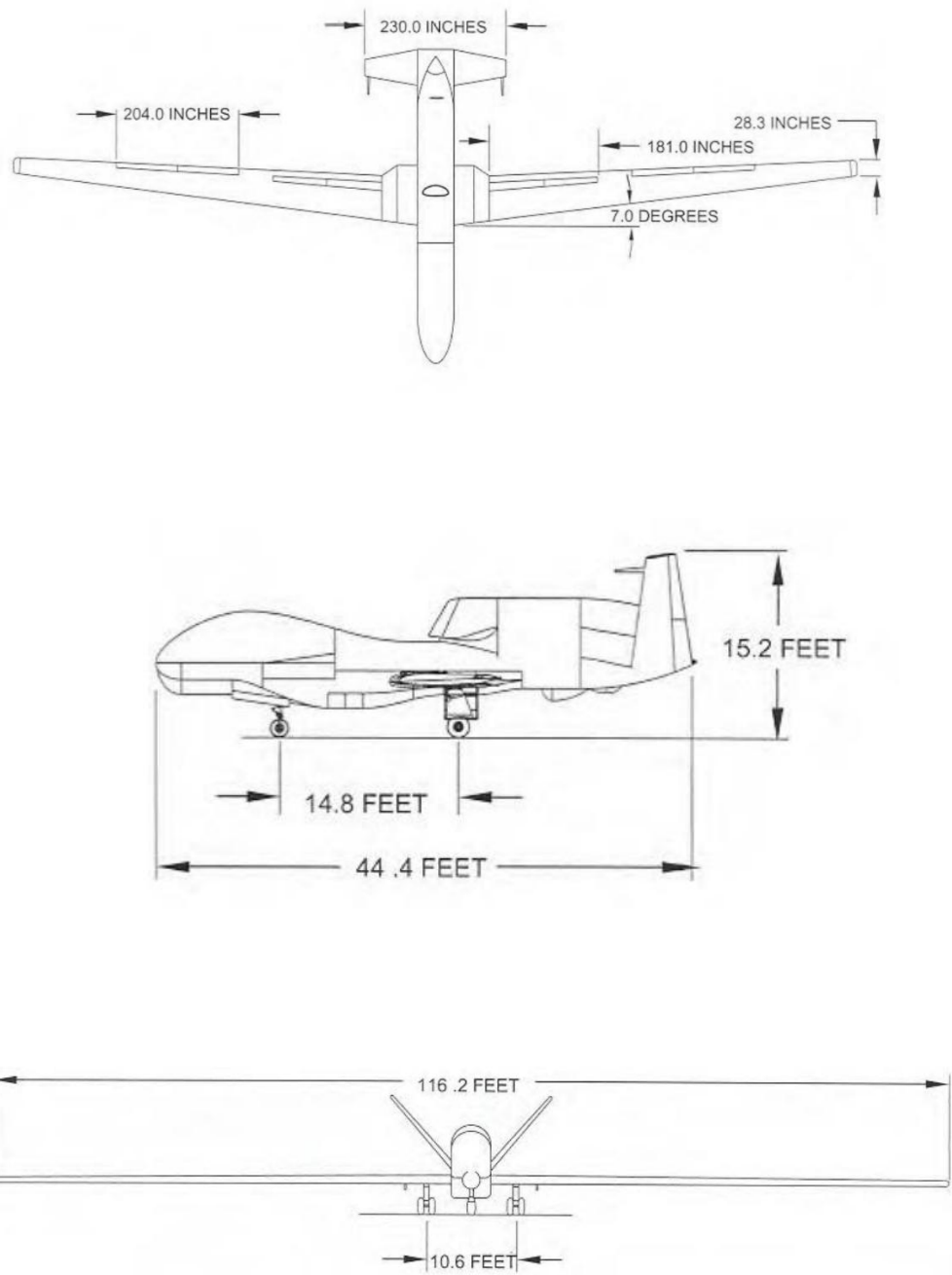


*Figure 3.2 Northrop Grumman RQ-4 Global Hawk reference.*

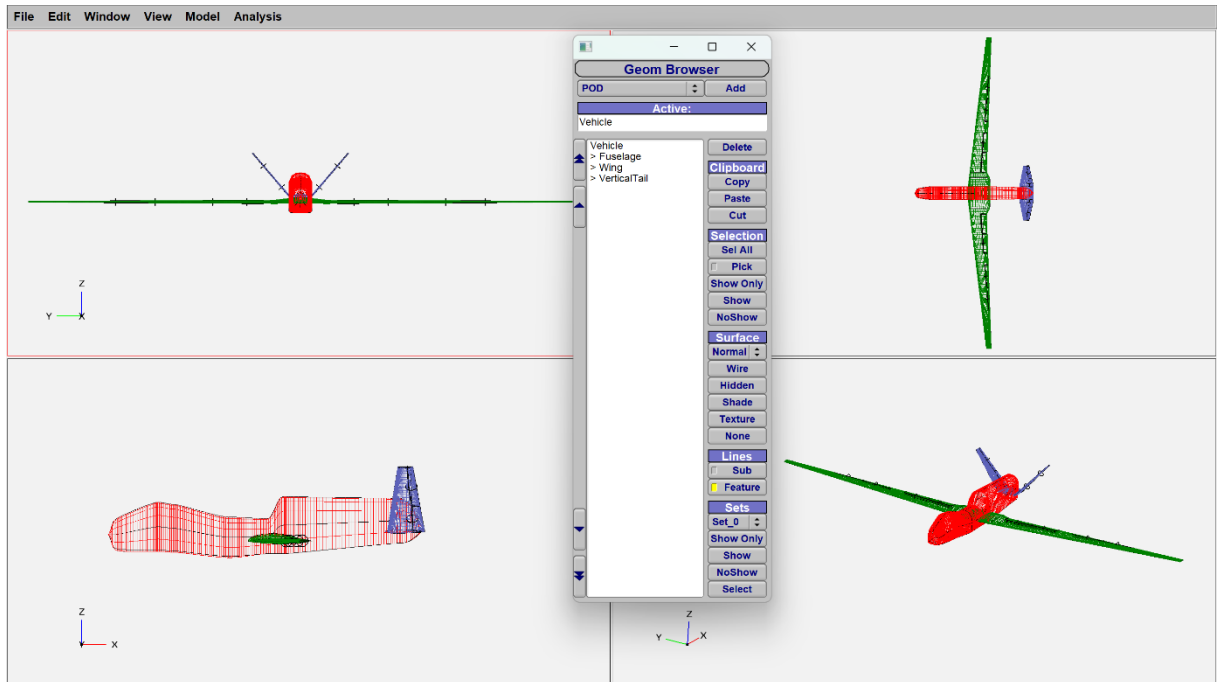


**Figure 3.3 GlobalHawk seen from four point of view in OpenVSP.**

### 3.2.1 Wing

The wing of the UAV has been designed as follows.

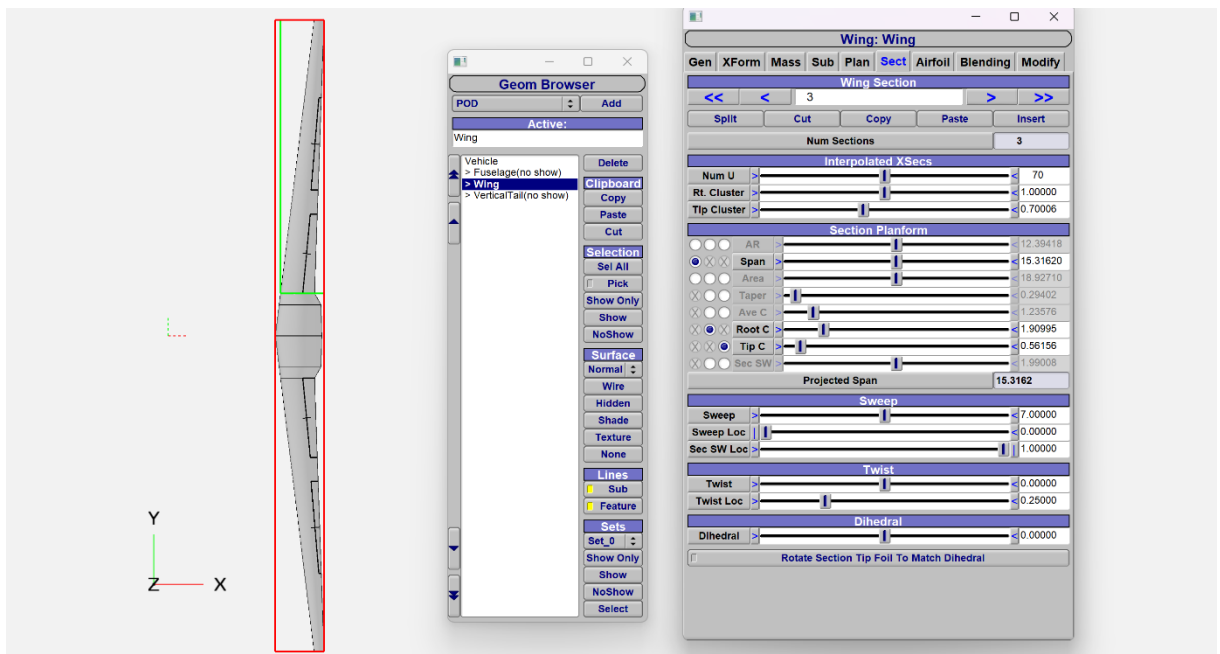


**Figure 3.4 Wing and wing geometry window.**

The wing has been split into three sections, each of which is characterized by a wing profile, depending on whether it is root, kink or tip. For the wing section, the NASA LRN 1015 airfoil [5] was assumed for the entire wingspan (Figure 3.5). Its parameters and performance have been obtained from the website <http://www.airfoiltools.com>.

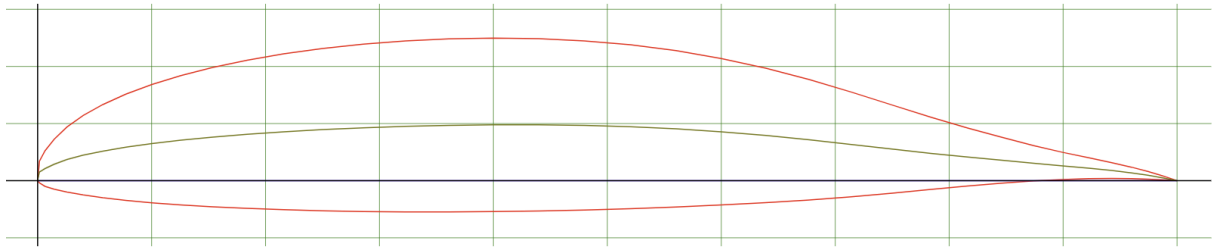


**Figure 3.5** Wing airfoil profile (NASA LRN 1015).

An assessment of the wing grid is made by adjusting the grid chordwise and spanwise. In both situations, the desired outcome is to obtain a pair of values U and W such that the polar curves derived from altering one of said parameters, while maintaining the other constant, reach an asymptotic trend, at a fixed angle of attack.

The first step is to adjust the grid chordwise by varying the W value using the tools made available in the wing geometry tab. To proceed with this first evaluation the U value has been set to the default setting of 16, and the angle of attack to 0°. We may conclude that the value of W=77 will suffice for the following studies.

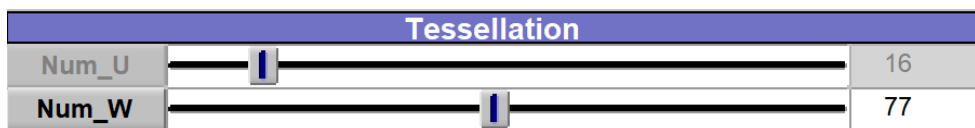


**Figure 3.6** Tessellation adjustment bar.

Considering the prior premise, the transverse direction refinement was accomplished by altering the U parameter in the wing geometry window Sect Tab, assuming now as fixed the previously found value of W. We may also take note of the fact that the wing model is made up of three sections, ergo the number of slices must be proportionally distributed between the three(Figure 3.7).

The pair of W and U values that are essential for building the grid are therefore  $W=77$  and  $U=40$ . The same grid will be used for the tailplane, in this way we can be consistent with how OpenVSP operates.

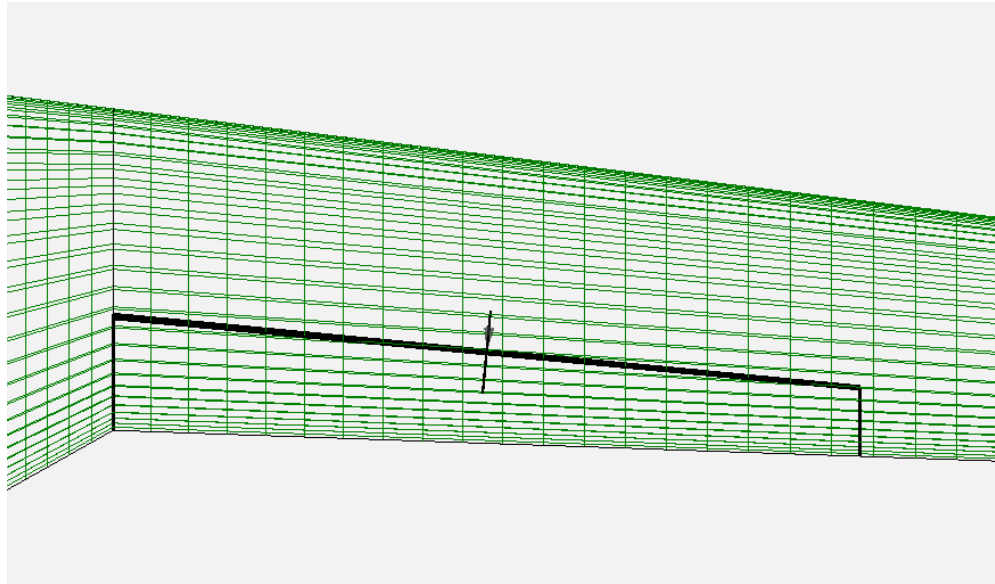


*Figure 3.7 Proportional distribution of the slices between section 2 and 3.*

### 3.2.2 Fuselage

The fuselage, like any other geometric component, has a geometric modelling window (Figure 3.8), which allows to enter the main measurements. It was possible to rebuild the curvature of the fuselage section by section by altering the parameter  $Z$  by displaying the design reference as a background to the design window. This fuselage structure has been divided into 8 sections.

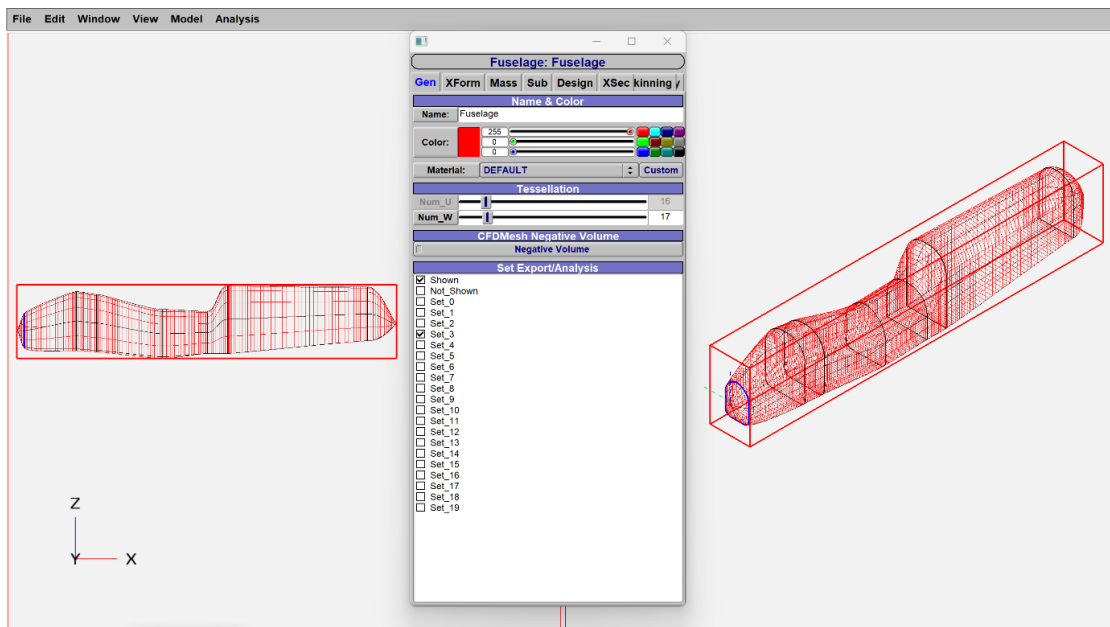


**Figure 3.8 Fuselage geometry window.**

### 3.2.3 V – Tailplane

The V-shape Tail basic geometric parameters need to be entered in the design window (Figure 3.9), using the same grid that was used for the wing. NACA 0010 airfoil (Figure 3.10) was chosen as the profile.

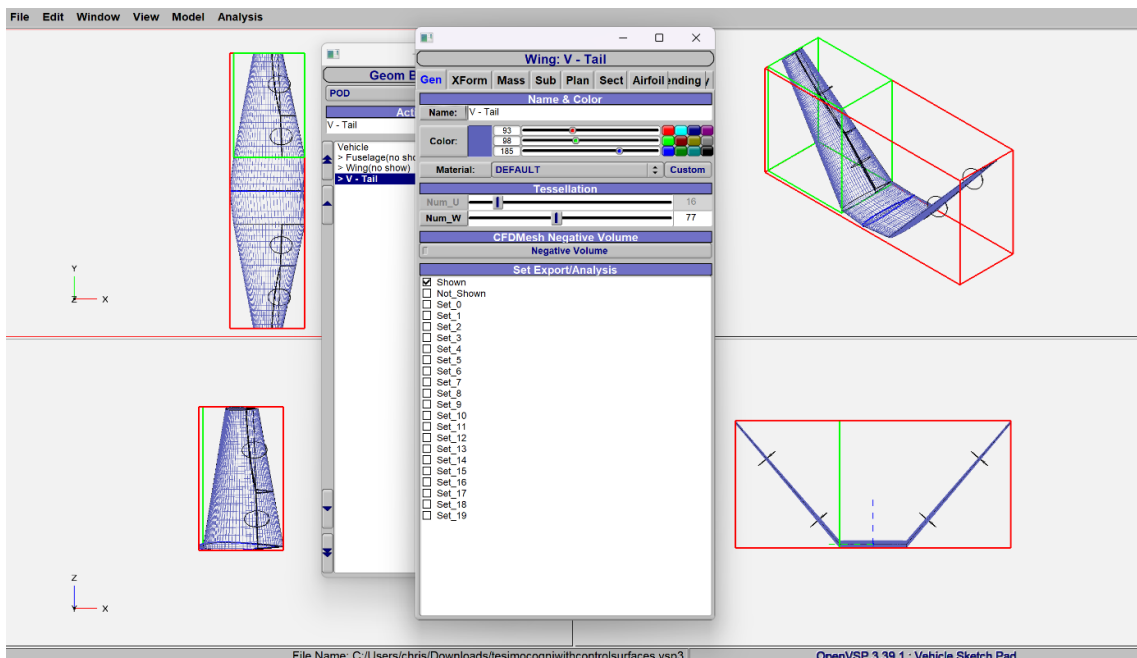


**Figure 3.9 Tailplane geometry window.**

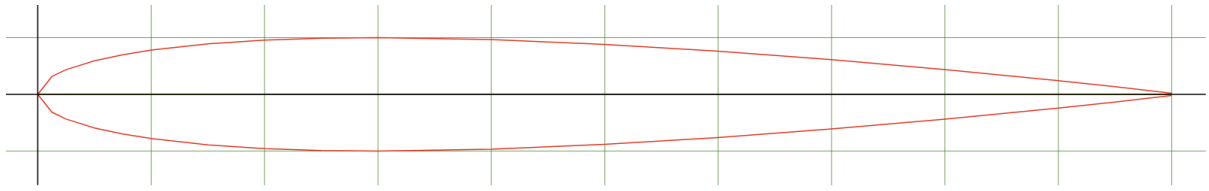


**Figure 3.10 Tailplane symmetrical airfoil profile (NACA 0010).**

## 4. Results and longitudinal aerodynamic analysis

As previously stated, the study was carried using the VSPAERO tool and using the Vortex Lattice Method (VLM). The user can select moment reference location and reference dimensions, or let the tool evaluate these quantities from the model.

References Area and lengths have been estimated from the model. Flow conditions were changed to have seven Alpha Start values, ranging to  $-2^\circ$  to  $10^\circ$ , Beta Start permanently null, Mach fixed at 0.6, and Reynolds number fixed at  $1E+07$ , according to RQ-4 Global Hawk cruise speed. The CG moment reference position was obtained by VSPAERO.

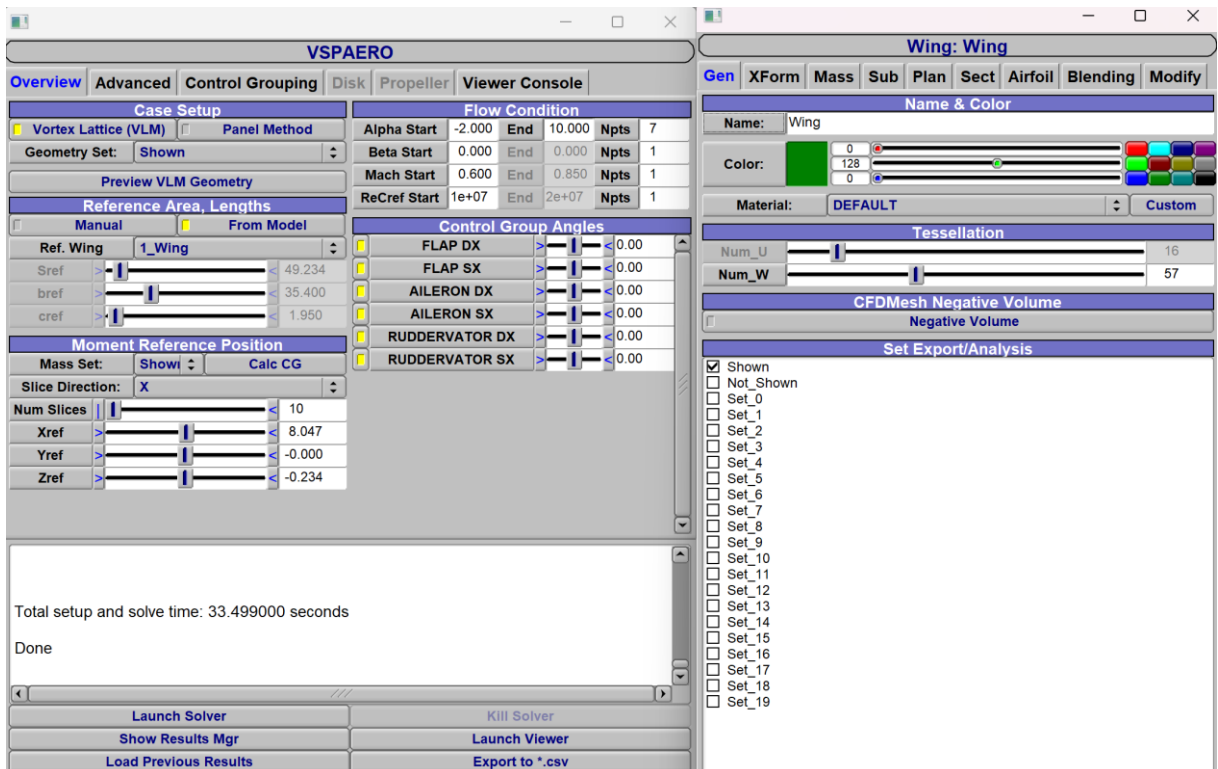


**Figure 4.1 VSPAero and set selection panels.**

Once the geometry of the airplane has been determined, we can proceed with the aerodynamic analysis of the contribution of each component, which can be done by selecting the desired set in VSPAero analysis panel.

All the subsequent calculations were carried out with Wing geometry fixed and the wind grid set up as previously mentioned. All control surfaces (Flaps, Ailerons and Ruddervators) are disabled for this analysis.

## 4.1 Aerodynamic curves

This section compares the 3D aerodynamic curves of an isolated wing (W), of the wing and tailplane combination (WT), and the of the entire aircraft.

$\alpha$	$C_{L_w}$	$C_{L_{wt}}$	$C_L$
-2°	0.360	0.294	0.336
0°	0.602	0.551	0.598
2°	0.843	0.809	0.863
4°	1.082	1.064	1.123
6°	1.320	1.318	1.385
8°	1.558	1.570	1.645
10°	1.791	1.820	1.909

*Table 4.1 Lift coefficients for the wing, wing and tail, complete aircraft.*

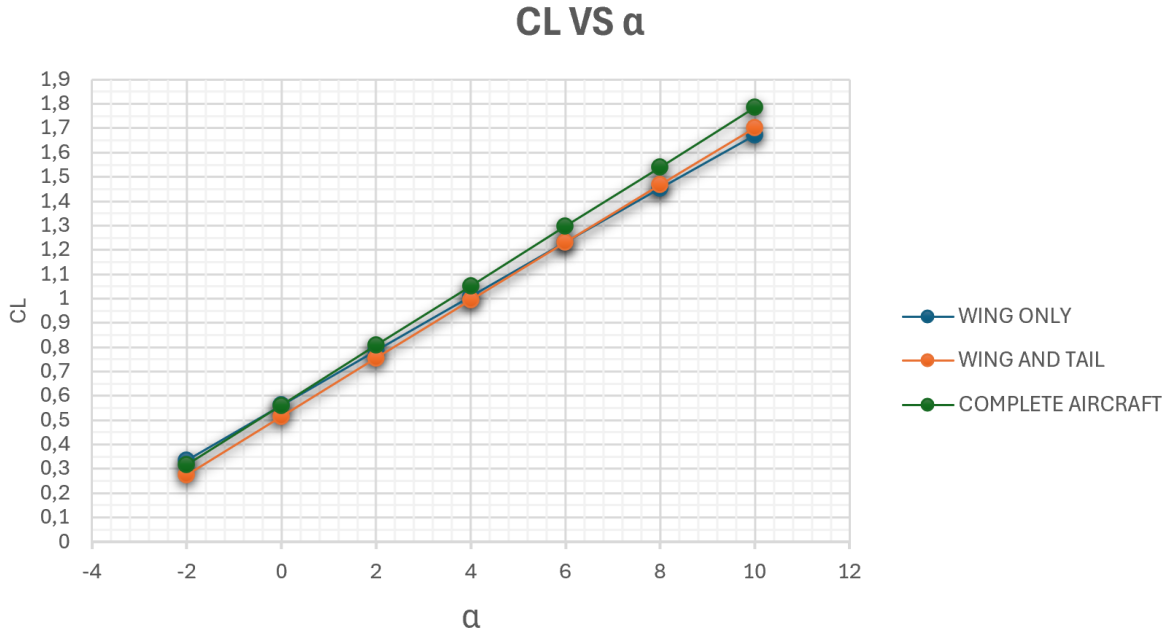


**Figure 4.2 Lift coefficient curves for the three sets of components.**

Because VSPAERO cannot execute stall conditions, the graph in Figure 4.2 only depicts the linear segment of a true lift coefficient curve.

It is clear that the fuselage has little impact on wing's lift properties. In facts, the linear behaviour is conserved in all situation examined.

Adding the fuselage and the tailplane, the slope of the  $C_{L\alpha}$  curve, as the added surface is load-bearing, but the reference area to normalize the coefficient remains the wing planform area  $S$ .

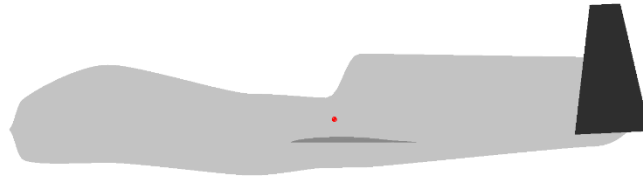
Using data from the previous table and the Excel SLOPE function, we can estimate useful derivatives for the three configurations. We can obtain  $C_{L\alpha}$ , which is the total aircraft's lift curve slope:

$$C_{L\alpha} = 0,122 \deg^{-1}. \quad \text{Equation 4.2}$$

To compute the pitching moment, the reference point (CG) must be assumed in VSPAERO.

CG coordinates are:  $X = 6.956 \text{ m}$ ;  $Y = 0 \text{ m}$ ;  $Z = 0.085 \text{ m}$

We can visualize the CG in Figure 4.3.



Vehicle CG: 6.955821, -0.000000, 0.085428

**Figure 4.3 Center of gravity of Global Hawk assumed in VSPAERO.**

$\alpha$	$C_{M_w}$	$C_{M_{wt}}$	$C_M$
-2°	-0.176	-0.007	-0.027
0°	-0.213	-0.083	-0.092
2°	-0.249	-0.161	-0.156
4°	-0.284	-0.238	-0.212
6°	-0.318	-0.312	-0.278
8°	-0.352	-0.386	-0.334
10°	-0.383	-0.461	-0.406

**Table 4.2** Pitching moment coefficients for the wing, wing and tail, complete aircraft.

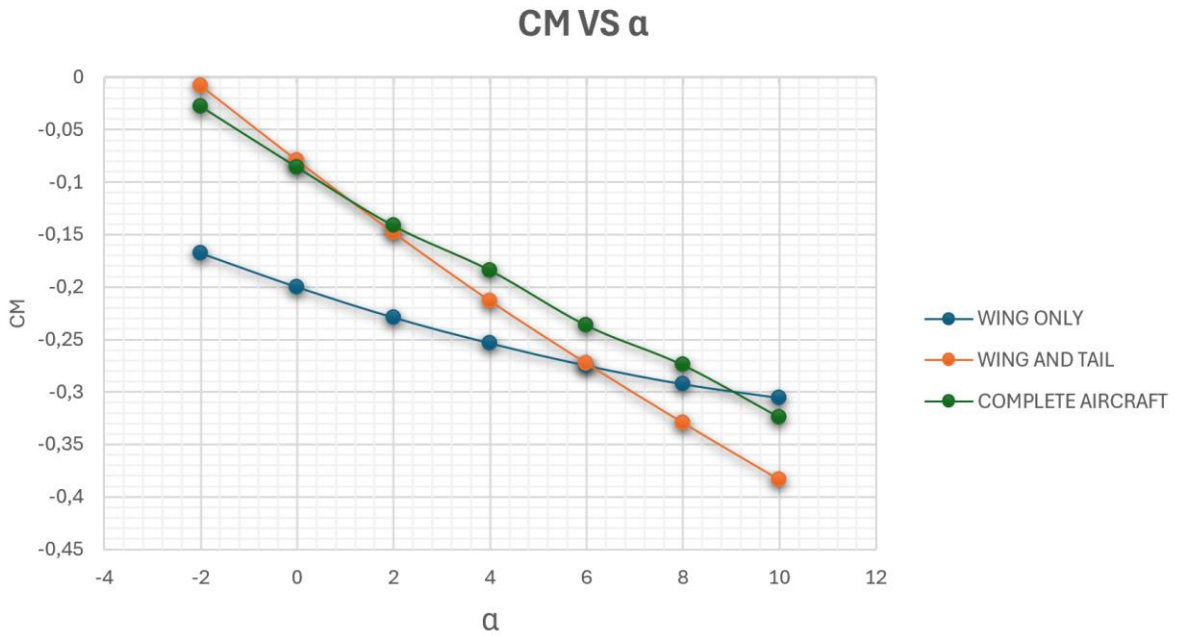


**Figure 4.4** Pitching moment coefficient curves.

Looking at Table 4.2 and Figure 4.4, for the pitching moment, it is apparent that the isolated wing exhibits a stable behaviour just as the wing body and the Global Hawk in its entirety. This is due to the location assumed for the reference point. The UAV in question is longitudinally stable with a negative  $C_{M\alpha}$  derivative.

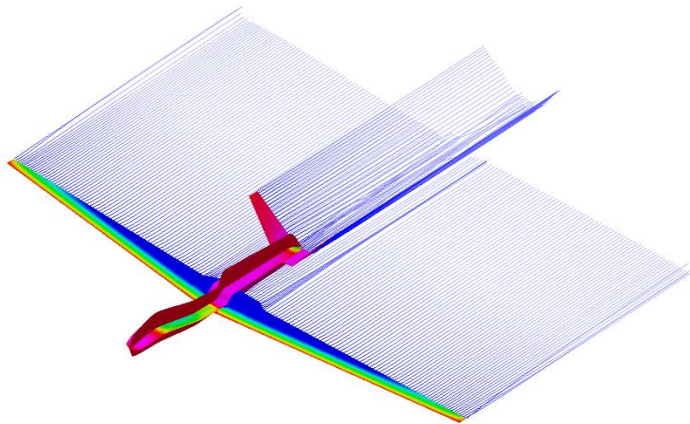


**Figure 4.5** Trailing wakes at  $\alpha = 4^\circ$ .

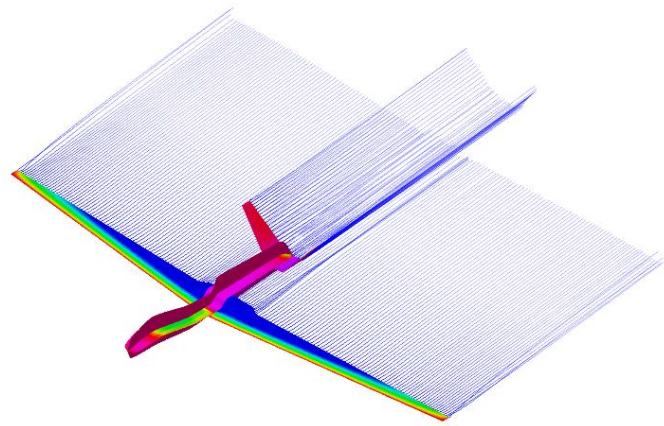


**Figure 4.6** Trailing wakes at  $\alpha = 8^\circ$ .

Exactly as done to find  $C_{L_\alpha}$ , we can obtain the pitching moment curve slope.

$$C_M_\alpha = -0,024 \deg^{-1}$$

**Equation 4.2**

which is negative, as expected from the table.

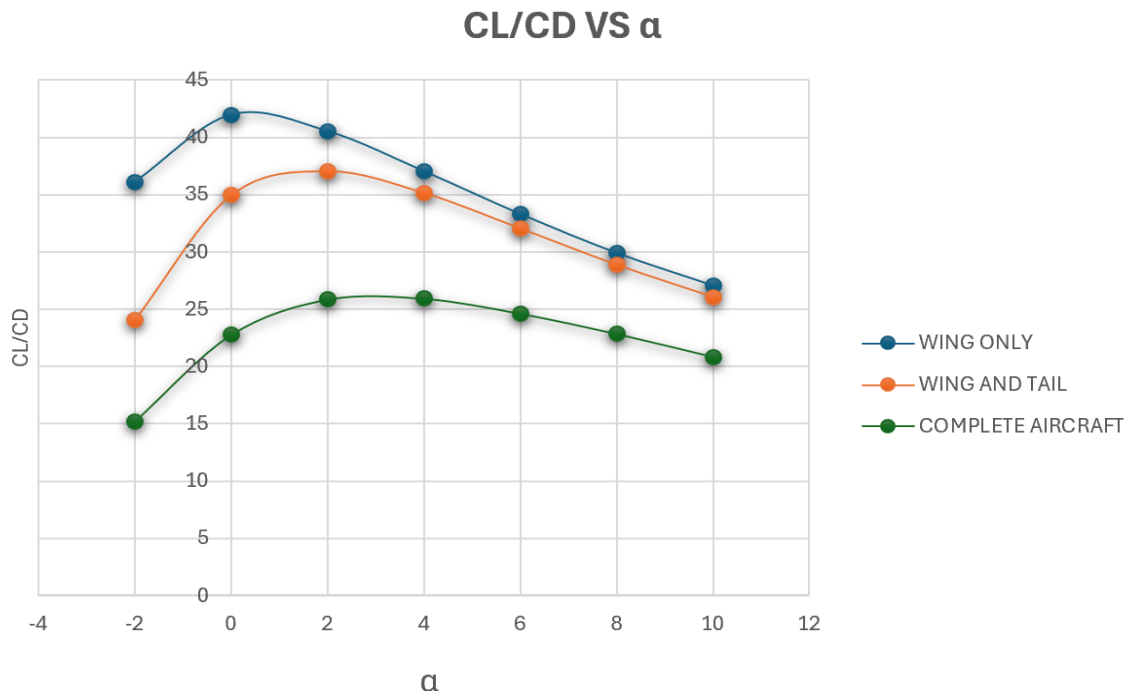


**Figure 4.7** Aerodynamic Efficiency curves

The addition of the fuselage leads the  $C_L/C_D$  efficiency curve to shift to lower values, owing to the increased parasite drag contribution.

Since VSPAERO provides only an approximation of the parasite drag with the flat plate approximation, this value has been calculated with the Parasite Drag Tool in OpenVSP.

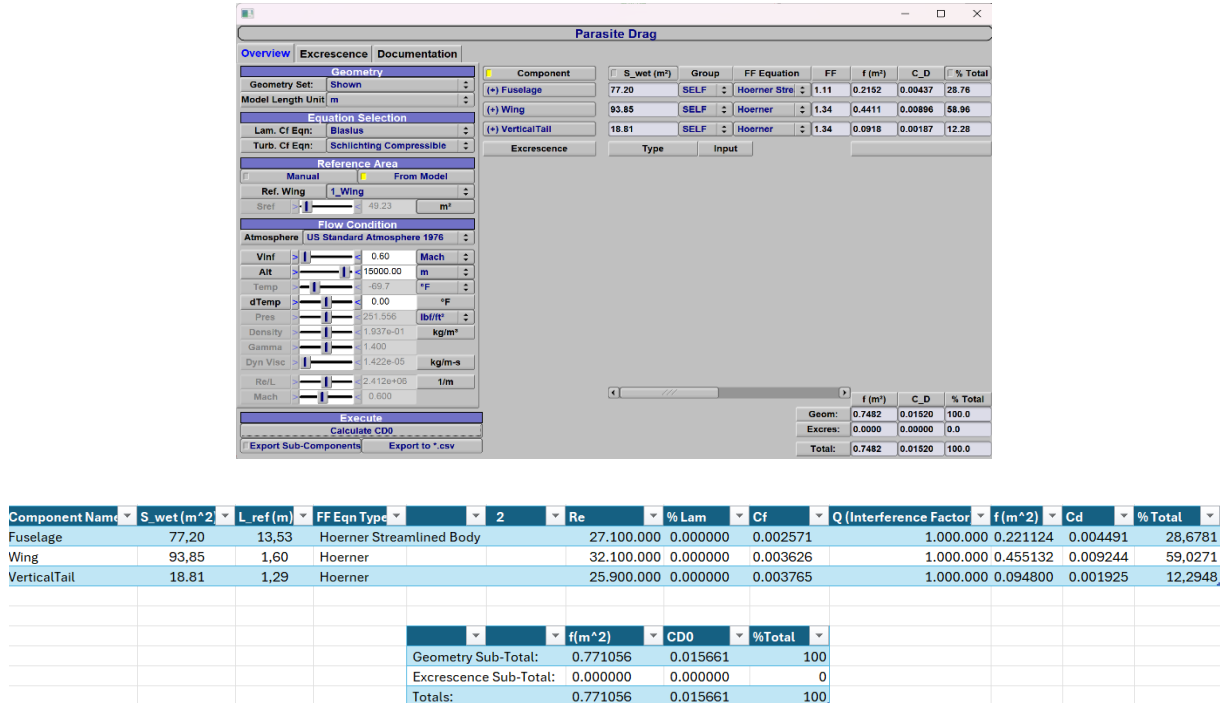


Figure 4.8 Parasite Drag tool results.

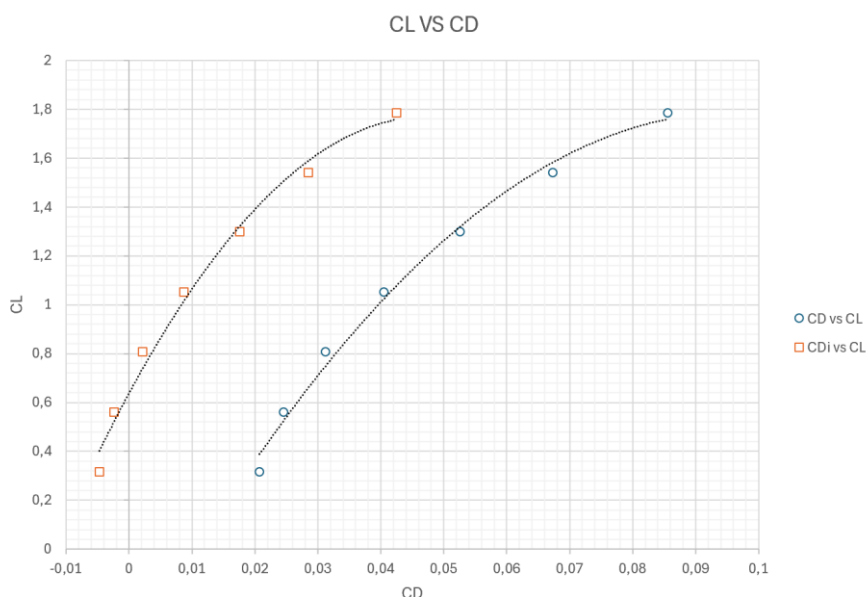


Figure 4.9  $C_L$  vs  $C_D$  and  $C_{Di}$  curves.

## 4.2 Neutral Point

To determine the neutral stability condition, the neutral point must be calculated. The first step is to linearize the aircraft pitching moment coefficient and set the equation linked to  $C_{M_\alpha}$  to zero:

$$C_{M_\alpha} = C_{L_{\alpha,W}} \cdot (\bar{X}_G - \bar{X}_{ac,WB}) - \eta_H \frac{s_H}{S} (\bar{X}_{ac,H} - \bar{X}_G) C_{L_{\alpha,H}} \left[ 1 - \left( \frac{d\varepsilon}{d\alpha} \right)_H \right] = 0 \quad \text{Equation 4.3}$$

At this point, the neutral point extended expression can be extracted by noting that when  $\bar{X}_G = \bar{X}_N$ , the airplane's pitch equilibrium is neutrally stable and assuming  $CL_{\alpha,WB} = CL_{\alpha,W}$ :

$$XN \equiv \frac{XN}{c} = \frac{\bar{X}_{ac,WB} + \eta_H C_{L_{\alpha,H}} \frac{s_H \bar{X}_{ac,WB} [1 - (d\varepsilon/d\alpha)_H]}{C_{L_{\alpha,WB}}}}{1 + \eta_H C_{L_{\alpha,H}} \frac{s_H [1 - (d\varepsilon/d\alpha)_H]}{C_{L_{\alpha,WB}}}} \quad \text{Equation 4.4}$$

The concept of static stability margin can be defined using the neutral point:

$$SM = \bar{X}_G - \bar{X}_N \quad \text{Equation 4.5}$$

Another valuable formulation for  $C_{M_\alpha}$  comes from the following equation:

$$C_{M_\alpha} = C_{L_\alpha} (\bar{X}_G - \bar{X}_N) = C_{L_\alpha} SM \quad \text{Equation 4.6}$$

Therefore, the neutral point location in fraction of the reference chord can be readily obtained from the slopes of the lift and pitching moment curve:

$$\bar{X}_N = \bar{X}_G - \frac{C_{M_\alpha}}{C_{L_\alpha}} = \frac{(6.956 - 6.000)m}{1.950 m} - \frac{-0.024 \deg^{-1}}{0.122 \deg^{-1}} = 0.490 + 0.197 = 0.687$$

where, at the second member, the first term is the nondimensional location of the center of gravity (reference point for the moments) and the second term is the nondimensional distance of the neutral point from the center of gravity, both given in fraction of reference chord. In our mathematical, linear model, the neutral point is located at about 68.7% of the mean chord.

### 4.3 Effects of control surfaces on Longitudinal Stability

The main goal of this analysis is to emphasize the effects of ruddervator deflection on the previously presented aerodynamic curves.

The control surfaces present on this aircraft include flaps, ailerons, and ruddervators (a combination of rudder and elevators).

The analysis of the deflection of these surfaces will be conducted at Mach = 0.001.

The ruddervators can deflect either symmetrically or asymmetrically. In the first case, they induce a rotation about the y-axis, altering the aircraft's longitudinal attitude. In the second case, asymmetric deflection affects the rolling moment, leading to a rotation about the x-axis. Due to the typical aerodynamic forces decomposition on the V-tail, this may also result in a change of the yawing moment.

The control surfaces present on this aircraft include flaps, ailerons, and ruddervators (a combination of rudder and elevators). The analysis of the deflection of these surfaces were conducted at Mach = 0.001.

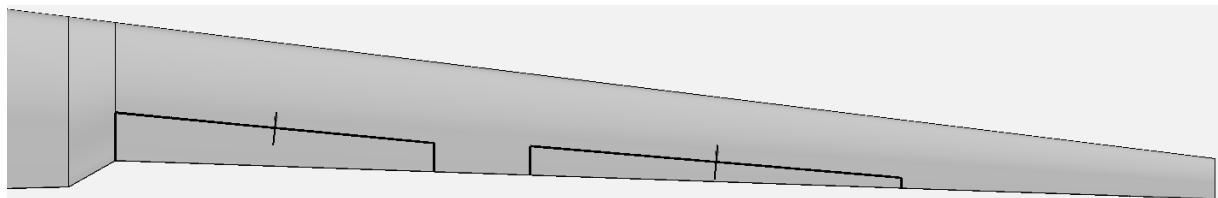


**Figure 4.10** Flaps and Ailerons.

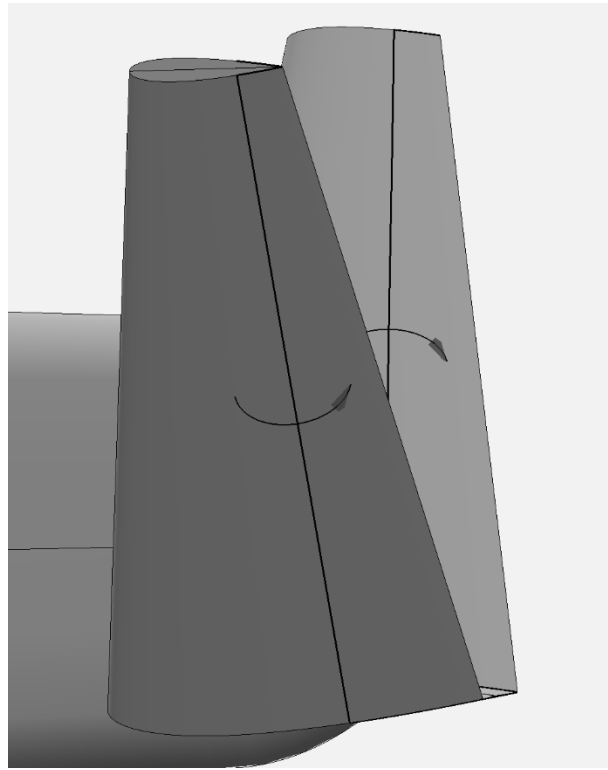


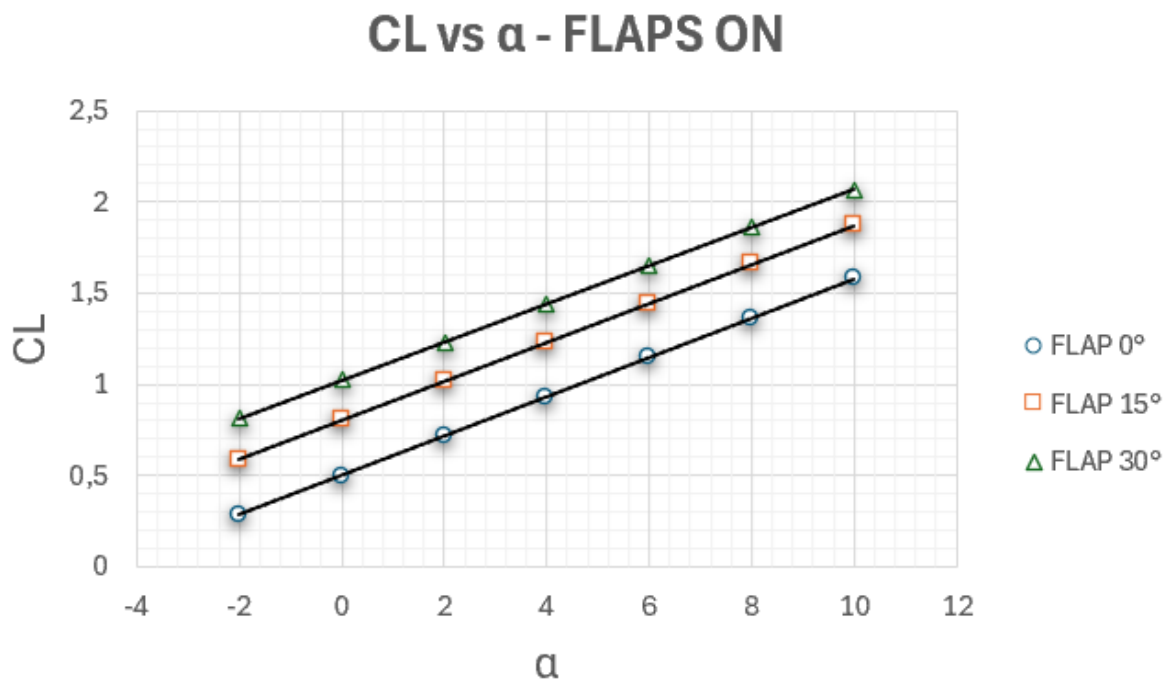
**Figure 4.11 Ruddervators.**

#### 4.3.1 Flaps

Flaps are control surfaces located on the wings of an aircraft, designed to modify lift and drag, particularly during takeoff and landing phases. When deployed, they increase the wing's camber, allowing the aircraft to generate greater lift at lower speeds. Simultaneously, they induce additional drag, which helps decelerate the aircraft and facilitates a controlled approach and landing. Various types of flaps exist, each with distinct aerodynamic characteristics, but they all serve the fundamental purpose of enhancing flight performance and safety during critical phases of operation.

The effects of flaps deflections at 0, 15°, and 30° on the lift coefficient are reported in Table 4.3 and Figure 4.122.

$\alpha$	$C_{L_{\delta f=0^\circ}}$	$C_{L_{\delta f=15^\circ}}$	$C_{M_{\delta f=30^\circ}}$
-2°	0.282	0.588	0.815
0°	0.498	0.802	1.023
2°	0.716	1.017	1.232
4°	0.929	1.227	1.439
6°	1.149	1.440	1.650
8°	1.361	1.657	1.860
10°	1.579	1.867	2.066

*Table 4.3 Lift coefficient for flap deflections of 0°, 15°, 30°.**Figure 4.12 Lift coefficient curves for flap deflections of 0°, 15°, 30°.*

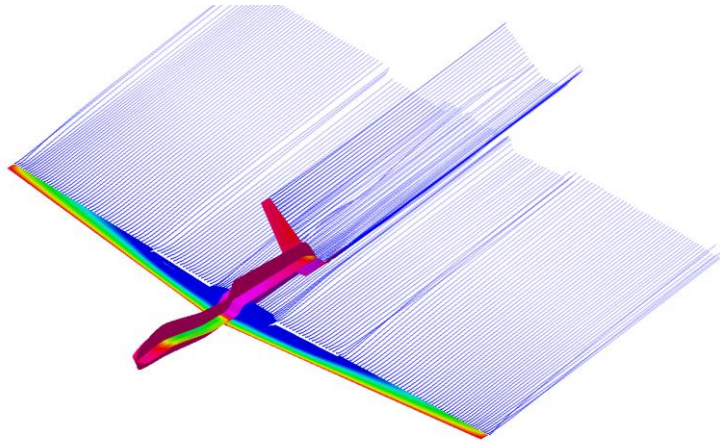


*Figure 4.13 Trailing wakes with flaps deflections of 15°.*

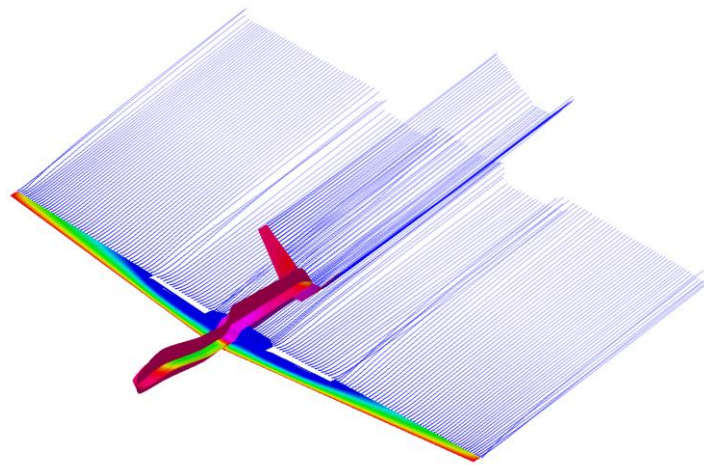


*Figure 4.14 Trailing wakes with flaps deflections of 30°.*

Control derivatives are aerodynamic coefficients that quantify the effect of control surfaces on aerodynamic forces and moments. They indicate how much a control surface influences the aircraft's dynamics in response to pilot inputs. Higher values suggest greater sensitivity and responsiveness. They are essential for analyzing flight stability and control. Their study enables the design of precise and efficient control systems.

We can estimate the control derivatives with the following formula:

$$C_{L_{\delta f}} = \frac{C_{L_{\delta f=15^\circ}} - C_{L_{\delta f=0^\circ}}}{\delta f - 0} \quad \text{Equation 4.11}$$

$$C_{L_{\delta f}} = 0,0203 \deg^{-1}. \quad \text{Equation 4.12}$$

Regarding the pitching moment coefficient, considering that the center of gravity position is the same as used to calculate the curves shown previously, the following data set is obtained:

$\alpha$	$C_{M_{\delta f=0^\circ}}$	$C_{M_{\delta f=15^\circ}}$	$C_{M_{\delta f=30^\circ}}$
-2°	-0.024	-0.054	-0.081
0°	-0.074	-0.106	-0.134
2°	-0.121	-0.160	-0.189
4°	-0.157	-0.201	-0.235
6°	-0.203	-0.252	-0.290
8°	-0.235	-0.315	-0.345
10°	-0.280	-0.365	-0.399

Table 4.4 Pitching moment coefficient values for flap deflections of 0°, 15° and 30°.

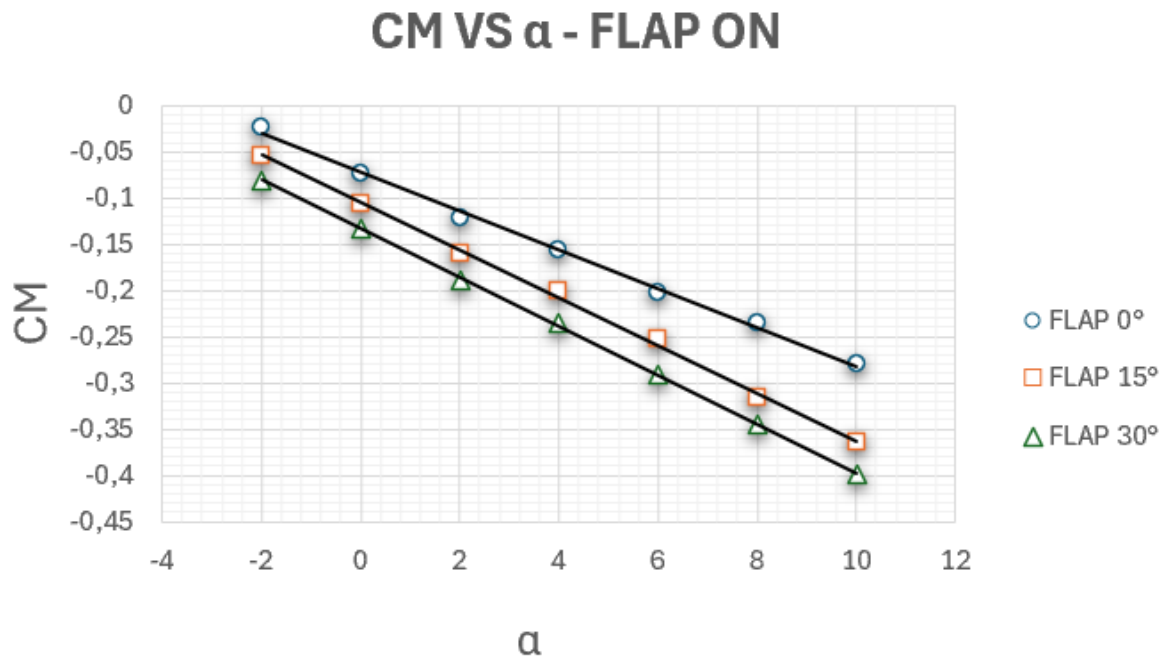


Figure 4.15 Pitching moment coefficient curves for flap deflections of 0°, 15° and 30°.

$$C_{M_{\delta f}} = -0,0021 \deg^{-1}. \quad \text{Equation 4.13}$$

#### 4.3.2 Ruddervators with symmetrical deflections

Ruddervators are aerodynamic control surfaces used on aircraft with a V-tail configuration. These surfaces integrate the functions of both the rudder and the elevator into a single control device installed on the inclined tailplanes. Symmetrical deflection occurs when both ruddervators move in the same direction and at the same angle. If the ruddervators deflect upward, they generate negative lift, pushing the tail downward and causing the aircraft's nose to rise. Conversely, if the ruddervators deflect downward, they generate positive lift, raising the tail and causing the nose to lower.

We can visualize this effect in Table 4.5 and Figure 4.16.

$\alpha$	$C_{L\delta r=0^\circ}$	$C_{L\delta r=10^\circ}$	$C_{L\delta r=-10^\circ}$	$C_{L\delta r=-20^\circ}$	$C_{L\delta r=-30^\circ}$
-2°	0.282	0.359	0.207	0.145	0.099
0°	0.498	0.576	0.423	0.359	0.312
2°	0.716	0.795	0.639	0.573	0.526
4°	0.929	1.004	0.854	0.781	0.729
6°	1.149	1.225	1.069	0.998	0.943
8°	1.361	1.441	1.285	1.213	1.159
10°	1.579	1.658	1.494	1.424	1.369

Table 4.5 Lift coefficient for ruddervators symmetrical deflections of +10°, 0°, -10°, -20° and -30°.

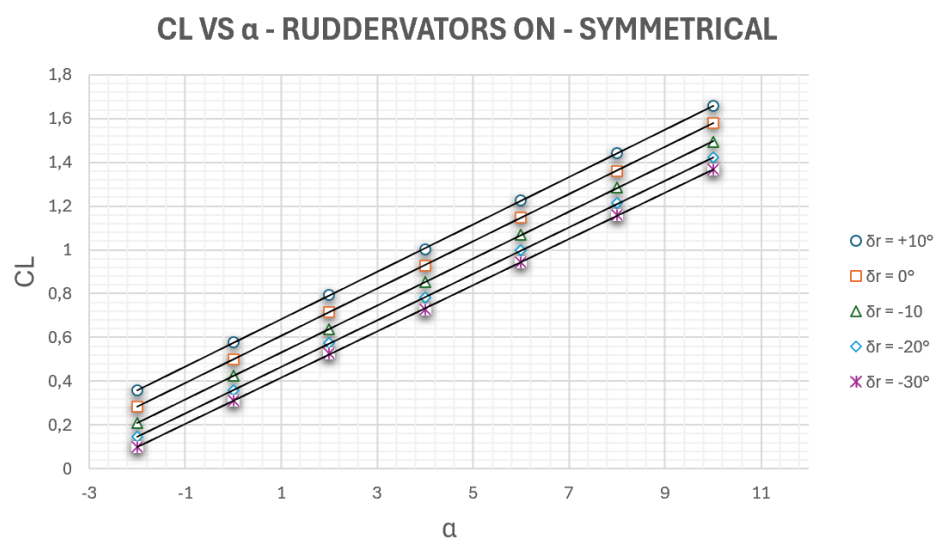
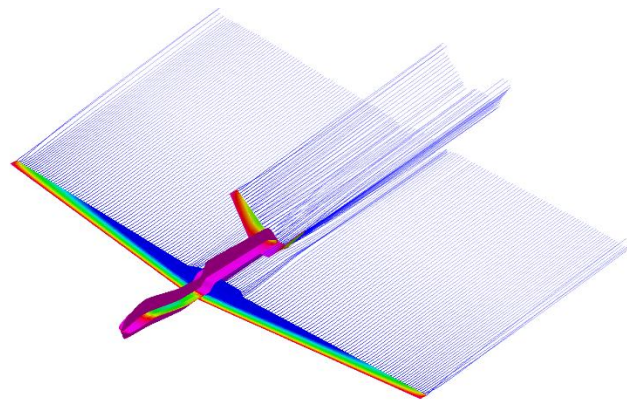
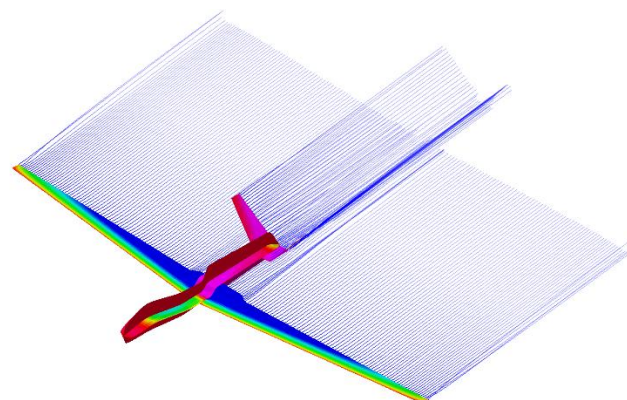


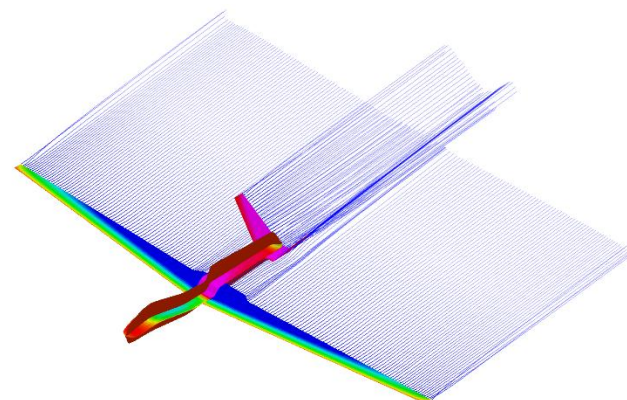
Figure 4.16 Lift coefficient curves for ruddervators symmetrical deflections of +10°, 0°, -10°, -20° and -30°.



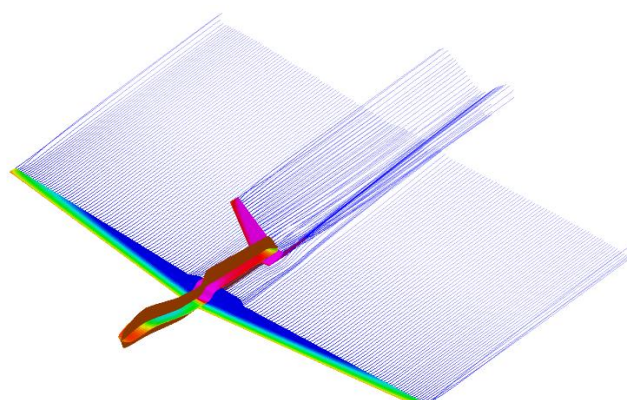
$\delta r = 10^\circ$



$\delta r = -10^\circ$



$\delta r = -20^\circ$



$\delta r = -30^\circ$

*Figure 4.17 Trailing wakes for ruddervators deflections, for each  $\delta r$ .*

$$C_{L\delta r} = 0,008 \text{ deg}^{-1}.$$

**Equation 4.14**

Regarding the pitching moment coefficient, considering that the center of gravity position is the same as used to calculate the curves shown previously, the following data set is obtained (Table 4.6):

$\alpha$	$C_{M\delta r=0^\circ}$	$C_{M\delta r=10^\circ}$	$C_{M\delta r=-10^\circ}$	$C_{M\delta r=-20^\circ}$	$C_{M\delta r=-30^\circ}$
-2°	-0.024	-0.225	0.180	0.351	0.480
0°	-0.074	-0.282	0.131	0.305	0.436
2°	-0.121	-0.340	0.083	0.261	0.394
4°	-0.157	-0.369	0.041	0.233	0.371
6°	-0.203	-0.430	-0.007	0.187	0.335
8°	-0.235	-0.482	-0.056	0.140	0.286
10°	-0.280	-0.539	-0.095	0.094	0.244

**Table 4.6 Pitching moment coefficient values for ruddervators symmetrical deflections of +10°, 0°, -10°, -20° and -30°.**

From these data, the diagram in Figure 4.18 can be obtained.

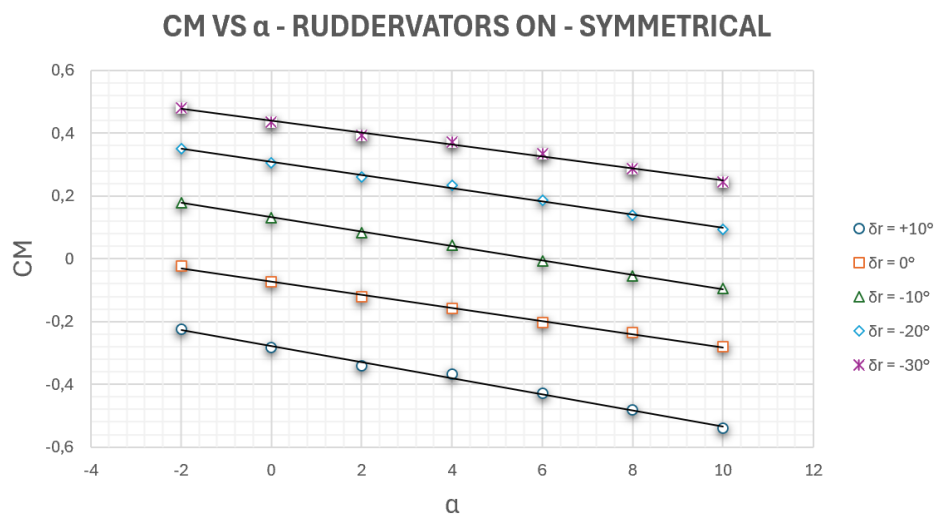


**Figure 4.18** Pitching moment coefficient curves for ruddervators symmetrical deflections of +10°, 0°, -10°, -20° and -30°.

$$C_{M\delta r} = 0,021 \text{ deg}^{-1}.$$

**Equation 4.15**

## 4.4 Lateral and Directional Stability Aerodynamics Analysis

The conditions applied for lateral and directional aerodynamic analysis are identical to those used for longitudinal analysis. However, in this case, the angle of attack  $\alpha$  is held constant while the sideslip angle  $\beta$  varies between  $-5^\circ$  and  $20^\circ$ , through steps of  $5^\circ$ . The coefficients analyzed will be  $C\ell$  (rolling moment) and  $C_n$  (yaw moment).

### 4.4.1 Aircraft behavior without control surfaces deflected

Without the use of control surfaces, the lateral and directional moments behave as illustrated in Table 4.7 and Figure 4.19. Naturally, due to the aircraft's symmetry, each coefficient remains minimal when  $\beta = 0$ . These small values are regarded as numerical errors resulting from the discretization of the model into a finite number of lattices.

$\beta$	$C_\ell$	$C_n$
$-5^\circ$	-0.001	0.0001
$0^\circ$	0.0003	-2e+07
$5^\circ$	0.002	0.001
$10^\circ$	0.003	0.001
$15^\circ$	0.005	0.001
$20^\circ$	0.006	0.002

Table 4.7 Natural Response of the aircraft with  $\beta$  variations.

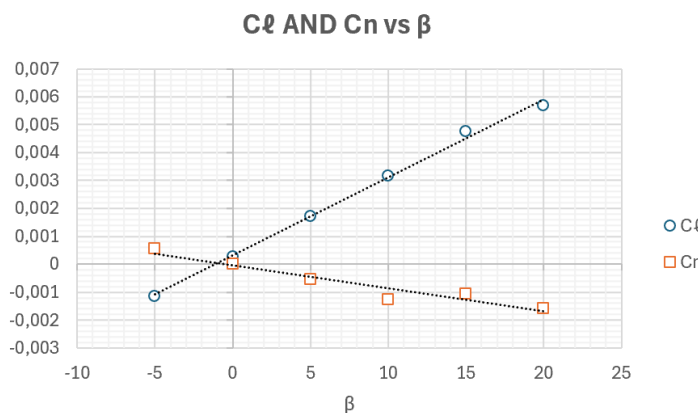


Figure 4.19 Lateral and Directional Natural Response of the aircraft with  $\beta$  variations.

#### 4.4.2 Ailerons effect on Lateral and Directional stability

Ailerons are control surfaces located on the trailing edge of an aircraft's wings, typically near the wingtips. They are responsible for controlling the rolling motion, which is the rotation of the aircraft around its longitudinal axis. Ailerons operate in pairs: when one is deflected upward, the other moves downward, creating a lift differential between the two wings. This induces a banked turn, allowing the aircraft to change direction efficiently. Ailerons are crucial for maneuverability, particularly during takeoff, landing, and turning, ensuring stability and precise control throughout the flight. The objective is to determine the control power.

Regarding the rolling moment, the analyses performed using VSPAERO have provided the following data (Table 4.8):

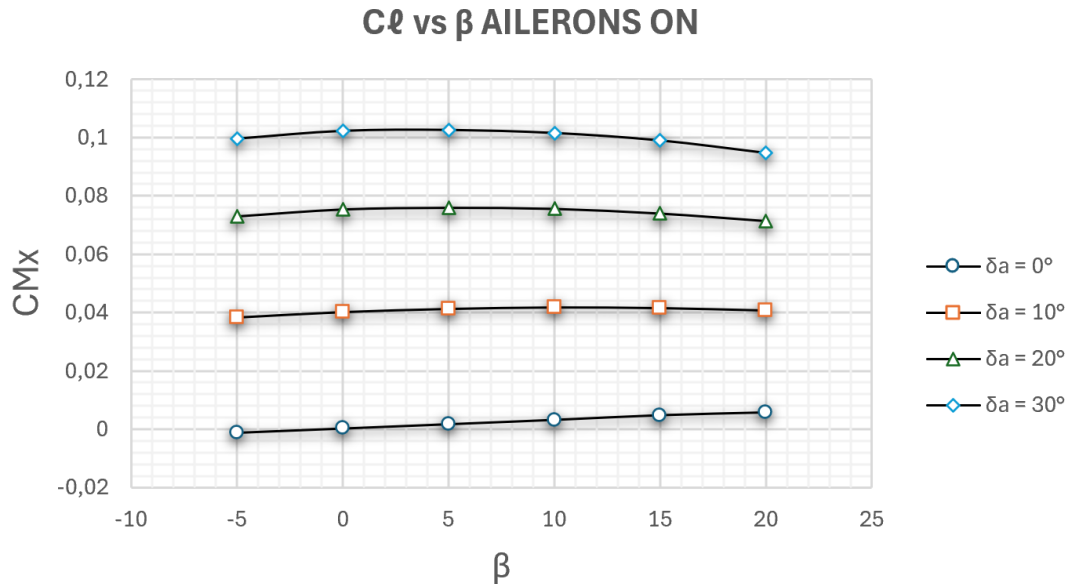
$\beta$	$C_{\ell_{\delta a=0^\circ}}$	$C_{\ell_{\delta a=10^\circ}}$	$C_{\ell_{\delta a=20^\circ}}$	$C_{\ell_{\delta a=30^\circ}}$
-5°	-0.0014	0.0383	0.0730	0.0996
0°	-0.0003	0.0401	0.0755	0.1023
5°	-0.0017	0.0412	0.0760	0.1026
10°	-0.0032	0.0417	0.0756	0.1016
15°	-0.0047	0.0415	0.0740	0.0990
20°	-0.0057	0.0407	0.0714	0.0947

**Table 4.8 Rolling moment coefficient with ailerons deflections of 0°, 10°, 20° and 30°.**

The estimated control derivative of ailerons is:

$$C_{\ell_{\delta a}} = 0.0038 \text{ deg}^{-1}. \quad \text{Equation 4.16}$$

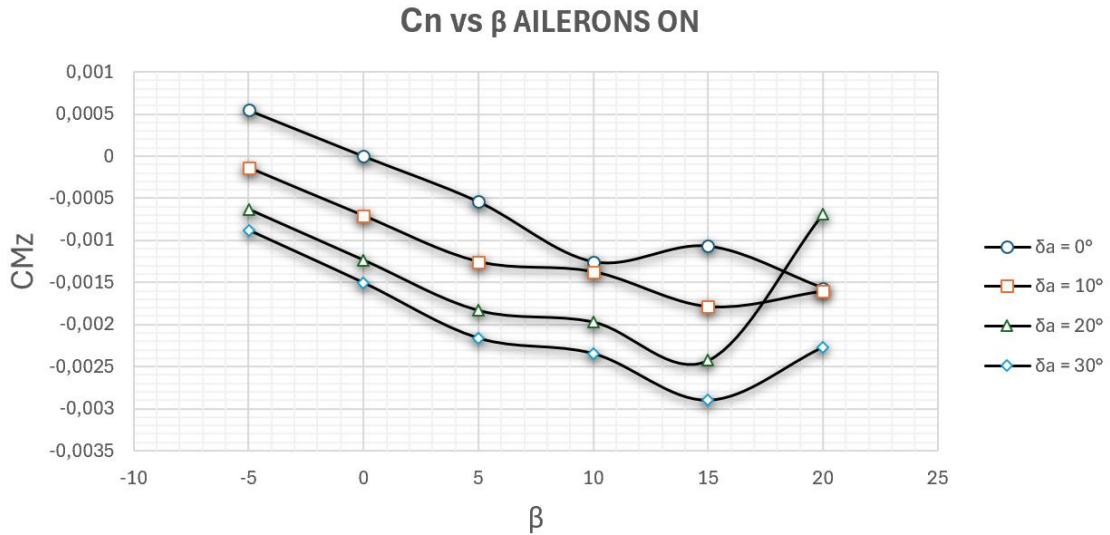
With these data, the following diagram can be constructed, allowing for the visualization of the curve trends for each deflection and, consequently, the control power can be estimated. (Figure 4.20)

**Figure 4.20**  $C\ell$  vs  $\delta a$ .

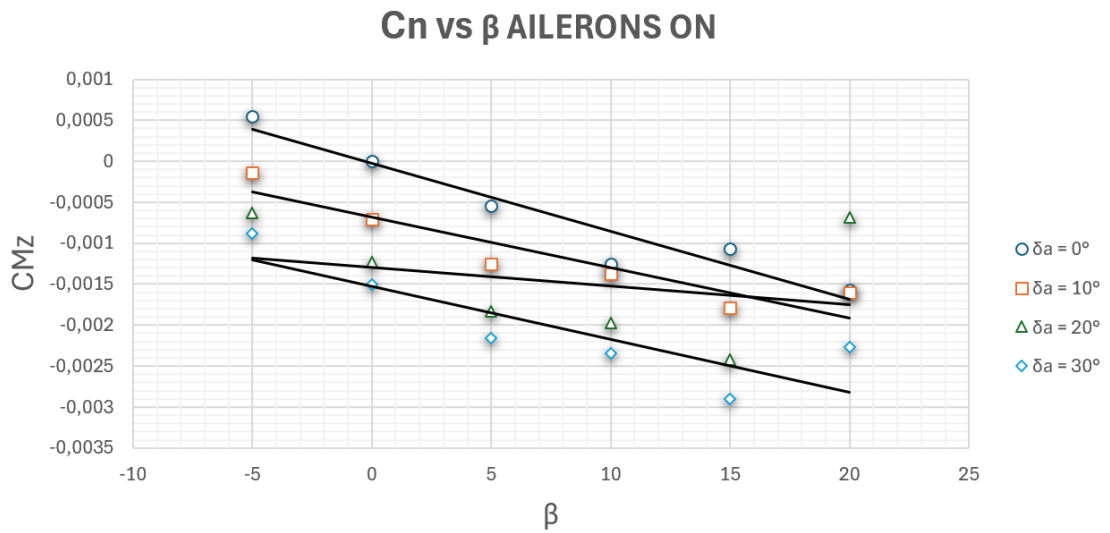
Regarding Yawing moment, looking at Table 4.9 and Figure 4.21 we can observe the aircraft behavior with ailerons deflections.

$\beta$	$C_{N_{\delta a=0^\circ}}$	$C_{N_{\delta a=10^\circ}}$	$C_{N_{\delta a=20^\circ}}$	$C_{N_{\delta a=30^\circ}}$
-5°	0.0005	-0.0001	-0.0006	-0.0009
0°	2.16e-07	-0.0007	-0.0012	-0.0015
5°	-0.0005	-0.0013	-0.0018	-0.0022
10°	-0.0013	-0.0014	-0.0019	-0.0023
15°	-0.0011	-0.0018	-0.0024	-0.0029
20°	-0.0016	-0.0016	-0.0007	-0.0023

**Table 4.9** Yawing moment coefficient with ailerons deflections of 0°, 10°, 20° and 30°.

**Figure 4.21**  $C_N$  vs  $\delta a$ .

Since VSPAero introduces calculation errors for the yawing moment coefficient at high aileron deflection angles, the control derivative is obtained by determining the trend line and restricting the calculation to segments where the curve can be approximated as a straight line (Figure 4.22), using Excel's SLOPE function (in this case, the lines exhibit a linear trend for  $\beta = -5^\circ$ ,  $\beta = 0^\circ$ , and  $\beta = 5^\circ$ ).

**Figure 4.22** Trend lines of  $C_N$  vs  $\delta a$ .

The estimated control derivative is:

$$C_{N\delta a} = -7.08 \times 10^{-5} \text{ deg}^{-1}.$$

**Equation 4.17**

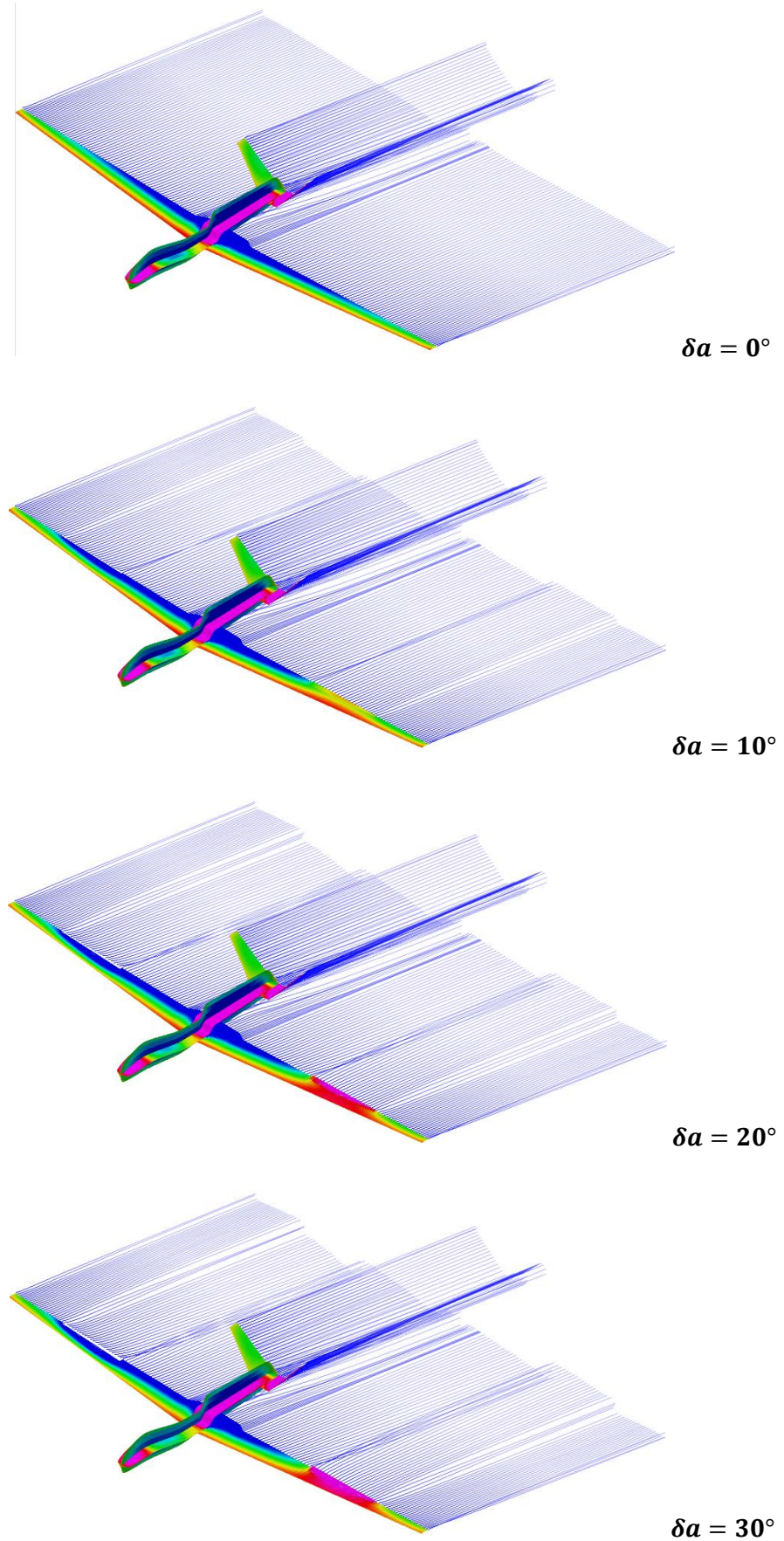


*Figure 4.23 Trailing wakes with ailerons deflections of  $0^\circ, 10^\circ, 20^\circ, 30^\circ$ .*

#### 4.4.3 Ruddervators effect on Lateral and Directional stability

As previously mentioned, when the ruddervators deflect asymmetrically, they generate both a rolling moment and a yawing moment. The objective is, once again, to determine the control power.

Regarding the Rolling moment, we obtained this set of values using VSPAero (Table 4.10):

Consequently, the diagram of Rolling moment with ruddervators deflections is displayed in Figure 4.24.

$\beta$	$C_{\ell_{\delta r=0^\circ}}$	$C_{\ell_{\delta r=10^\circ}}$	$C_{\ell_{\delta r=20^\circ}}$	$C_{\ell_{\delta r=30^\circ}}$
-5°	-0.0011	0.0029	0.0064	0.0092
0°	-0.0003	0.0045	0.0083	0.0111
5°	-0.0017	0.0059	0.0096	0.0122
10°	-0.0032	0.075	0.0108	0.0131
15°	-0.0047	0.0087	0.0119	0.0142
20°	-0.0057	0.0094	0.0125	0.0146

**Table 4.10 Rolling moment coefficient with ruddervators asymmetric deflections of 0°, 10°, 20° and 30°.**

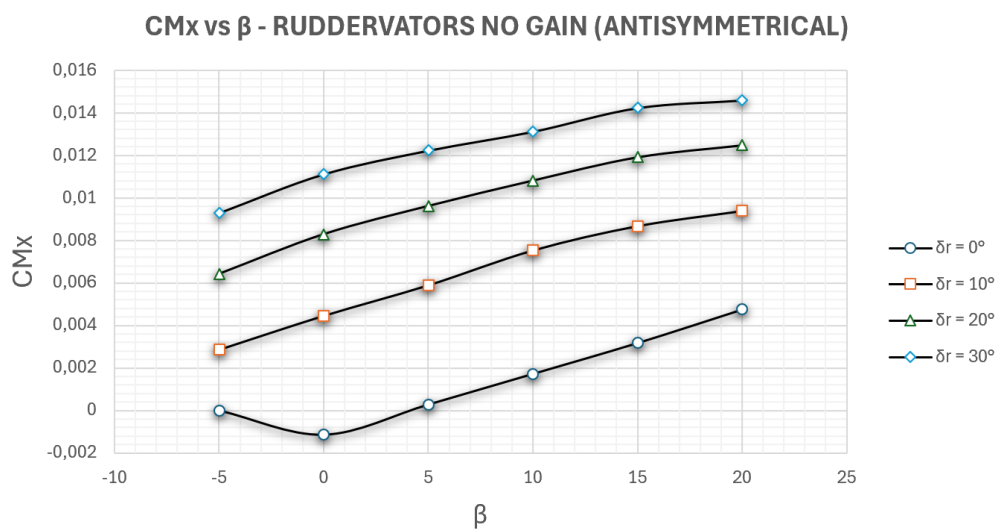


**Figure 4.24  $C_{\ell}$  vs  $\delta r$ .**

The estimated control derivative is:

$$C_{\ell_{\delta r}} = 0.00042 \text{ deg}^{-1}.$$

**Equation 4.18**

Regarding the Yawing moment, in Table 4.11 and Figure 4.25 we can see the way  $C_N$  changes with ruddervators deflections of  $0^\circ$ ,  $10^\circ$ ,  $20^\circ$  and  $30^\circ$ .

$\beta$	$C_{N_{\delta a=0^\circ}}$	$C_{N_{\delta a=10^\circ}}$	$C_{N_{\delta a=20^\circ}}$	$C_{N_{\delta a=30^\circ}}$
-5°	0.0005	-0.0075	-0.0145	-0.0204
0°	2.16e-07	-0.0081	-0.0152	-0.0207
5°	-0.0005	-0.0085	-0.0153	-0.0205
10°	-0.0013	-0.0083	-0.0147	-0.0198
15°	-0.0011	-0.0086	-0.0151	-0.0199
20°	-0.0016	-0.0090	-0.0152	-0.0197

**Table 4.11 Yawing moment coefficient with ruddervators asymmetric deflections of  $0^\circ$ ,  $10^\circ$ ,  $20^\circ$  and  $30^\circ$ .**

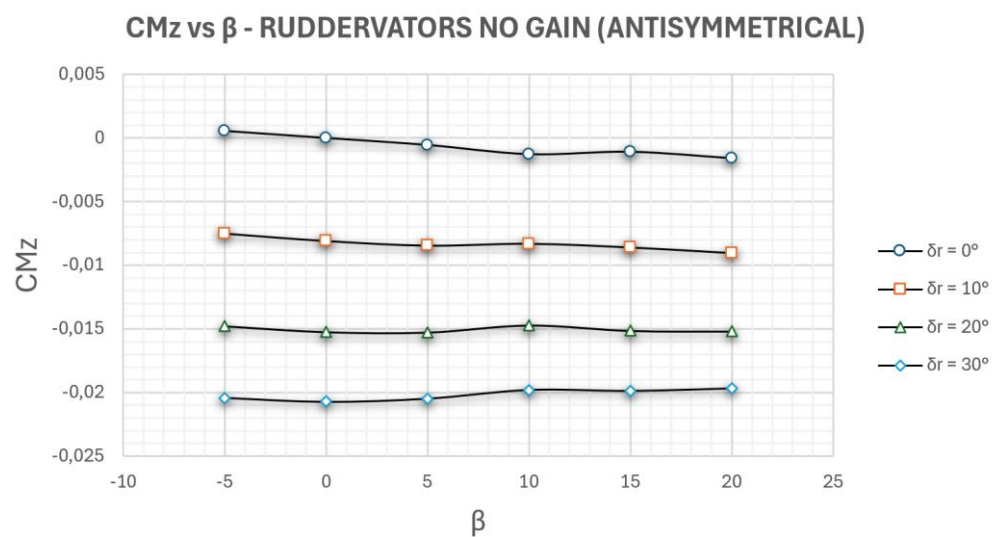


**Figure 4.25  $C_N$  vs  $\delta r$ .**

The estimated control derivative is:

$$C_{N_{\delta_r}} = 0.00081 \text{ deg}^{-1}. \quad \text{Equation 4.19}$$

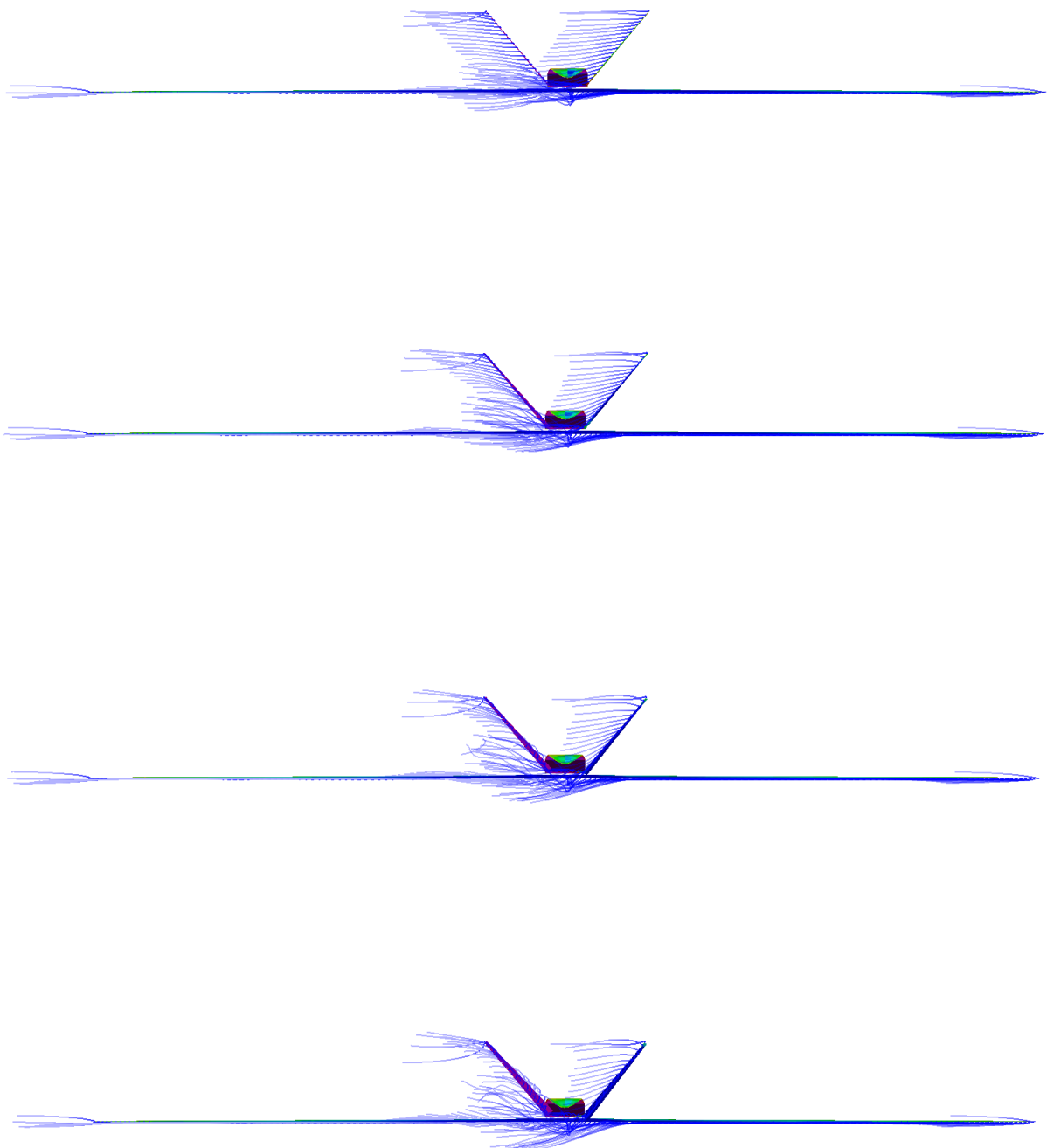


*Figure 4.26 Rear view of Trailing wakes for Ruddervators Antisymmetrical deflections of 0°, 10°, 20°, 30°.*

## 5. Conclusion

In this thesis, a geometric modeling project of the Global Hawk, an unmanned aerial vehicle (UAV), was conducted using OpenVSP software. Its particular shape, with its 35 meters wingspan, the unusual shape of the fuselage, represented a significant challenge. Then, a thorough aerodynamic analysis was carried out using VSPAERO, with the aim of confirm stability and controllability.

The aerodynamic analysis conducted with VSPAERO provided crucial results regarding the flight behaviour of the redesigned Global Hawk. Once the aerodynamic coefficients were calculated, the focus was on assessing the aircraft's stability and controllability, looking in depth at how control surfaces change the aerodynamic parameters. It is important to note, however, that some of the aerodynamic analyses conducted with VSPAERO are affected by a certain margin of numerical error. This is because the software approximates calculations by complex numerical methods, not performing them completely accurately. In addition, VSPAERO is unable to recognize some phenomena (such as aerodynamic stall).

The geometric modelling of the Global Hawk and the subsequent aerodynamic analysis have highlighted the importance of an integrated approach in the design of complex aircraft. The challenge of the unique shape of the Global Hawk has been overcome, demonstrating the potential of OpenVSP and VSPAERO for design optimization and performance verification. The stability and controllability of the aircraft, confirmed by the results obtained, are fundamental elements for the success of the missions the Global Hawk was designed for. While recognizing the limitations of the numerical approximation of VSPAERO, the results obtained still provide valuable information on the aerodynamic behavior of the Global Hawk modelled in this work.

## Bibliography

- [1] M. Person, (Oct 2, 2019). Global Hawk High-Altitude Long-Endurance Aircraft. *NASA*
- [2] Pascual Marqués, Andrea Da Ronch, Advanced UAV aerodynamics, Flight stability and control, John Wiley & Sons, Apr 27,2017.
- [3] NASA. (1976). Vortex Lattice Utilization. Hampton, Virginia, United States of America.
- [4] 2020 VSP WS: VSPAERO Theory, Validation, and Features <https://www.youtube.com/watch?v=zQEmmrB6ck> .
- [5] AirfoilTools Global Hawk page: <http://airfoiltools.com/airfoil/details?airfoil=lrn1015-il>
- [6] Reg Austin, Unmanned Aircraft Systems: UAVS Design, Development and Deployment, John Wiley & Sons, Sep 20, 2011.
- [7] OpenVSP website: <https://openvsp.org> .
- [8] Airfoiltools website: <http://www.airfoiltools.com> .